K-872352

Contents

4

List of Figures

8

List of Tables

Acknowledgements

If I were to acknowledge everyone who ever helped me on the work leading to this thesis, It would take almost as much time and paper as the thesis itself. Of course, it would be more fun to write. Several people, however, thoroughly deserve to be named in here, so I'll start rattling off a list, in no particular order:

I think every student who worked at the VTF group helped in some way. I'll spare the reader an exhaustive list here, but I feel thoroughly obligated to mention two names. Randy West, the VTF Vacuum God, devoted an incredible amount of his time helping me with machining, and even more time trying to get my experiment through some serious vacuum problems. In addition, I am very grateful to him for telling me exactly how idiotic some of my early ideas were, saving me much embarrassment. Jenise Bushman spent most of a summer building amplifier circuits for my experimental setup. Without her help, I would not have finished this thesis until next term.

Dexter Beals, Dan Moriarty, and Chris Rost, our trio of guitar-playing grad students, helped me out more times than I can remember.

More overflowing gratitude must be doled out to Bob Childs, head of the Alcator Vacuum Lab, whom I terrorized for months to help me with my vacuum design and construction... and reconstruction.

Engineers Dave Gwinn and Bill Byford actually came in to the lab on a Sunday to fix a magnet transformer so I could take some last-minute measurements a week before this thesis was due.

Peter Dandridge Sr. of Atomic, Ltd. is the greatest arc-welder in the world.

Marcel Gaudreau, the quintessential engineer, was the driving force behind the VTF group's founding and remains instrumental in its functioning. No thesis has ever been prepared here without his help.

Almost two years ago, Stan Luckhardt, the supervisor for this thesis, decided to hire me for some reason. Many requisitions and UROP proposals later, I am grateful to him for letting me take on such a large project and for his help along the way.

I have to thank Ron Parker for many things, particularly for not killing me on a certain day in July 1992, when I interrupted a meeting with D.O.E. funding officials to ask for his signature on a $26 requisition.

I should also mention my neighbors in MacGregor House, who provided the perfect balance of support and derision to get me through the ordeal of writing this thing.

This thesis is dedicated to a generic UROP student who knows why $\Gamma\Phi = 3\cos\omega t$.

An Introductory Note: Unit Conventions

In writing this thesis, I have attempted to present all equations and results in the Gaussian (cgs) unit system. There are two main exceptions to this. Section 3.1 is essentially an engineering description of the equipment built for the experiments described in the following chapters. Because of American equipment and machining standards, many of the parts I obtained were machined to standard English sizes. It would have been very awkward to convert to centimeters many of the dimensions involved, and so I have left the entire equipment description in inches.

A more subtle violation of the cgs standard occurs in Chapters 4 and 5, where electrical potential is generally measured in volts rather than statvolts, the cgs unit. Wherever the difference presents a problem in calculations, a conversion is given as well.

Chapter 1

The Versatile Toroidal Facility

The Versatile Toroidal Facility (VTF) at the MIT Plasma Fusion Center (PFC) is a toroidal plasma chamber designed for fundamental plasma physics experiments. Its construction began in 1988 with the acquisition of eighteen magnetic coils from the Oak Ridge National Laboratory. An aluminum support structure and stainless steel vacuum chamber were designed and partially constructed by a group of students in 1989 and 1990 under the supervision of Dr. Marcel Gaudreau. The vacuum chamber was built at Atomic, Ltd., in Cambridge.[1] In recent years, the facility has been used as a low-density plasma chamber. At present, it is being upgraded to achieve a higher plasma density by injection of an electron beam.

1.1   VTF Vacuum Chamber

The chamber itself is a torus with a rectangular cross-section. It has an outer radius of 125.7 cm, an inner radius of 59.7 cm, and a height of 105.4 cm (see Figure 1-2), making

---

[1]Beals, D. F.: *Vacuum System Construction and Analysis for a TOKAMAK Plasma Device*, S. B. Thesis, Department of Mechanical Engineering, MIT, Cambridge, Mass., 1991
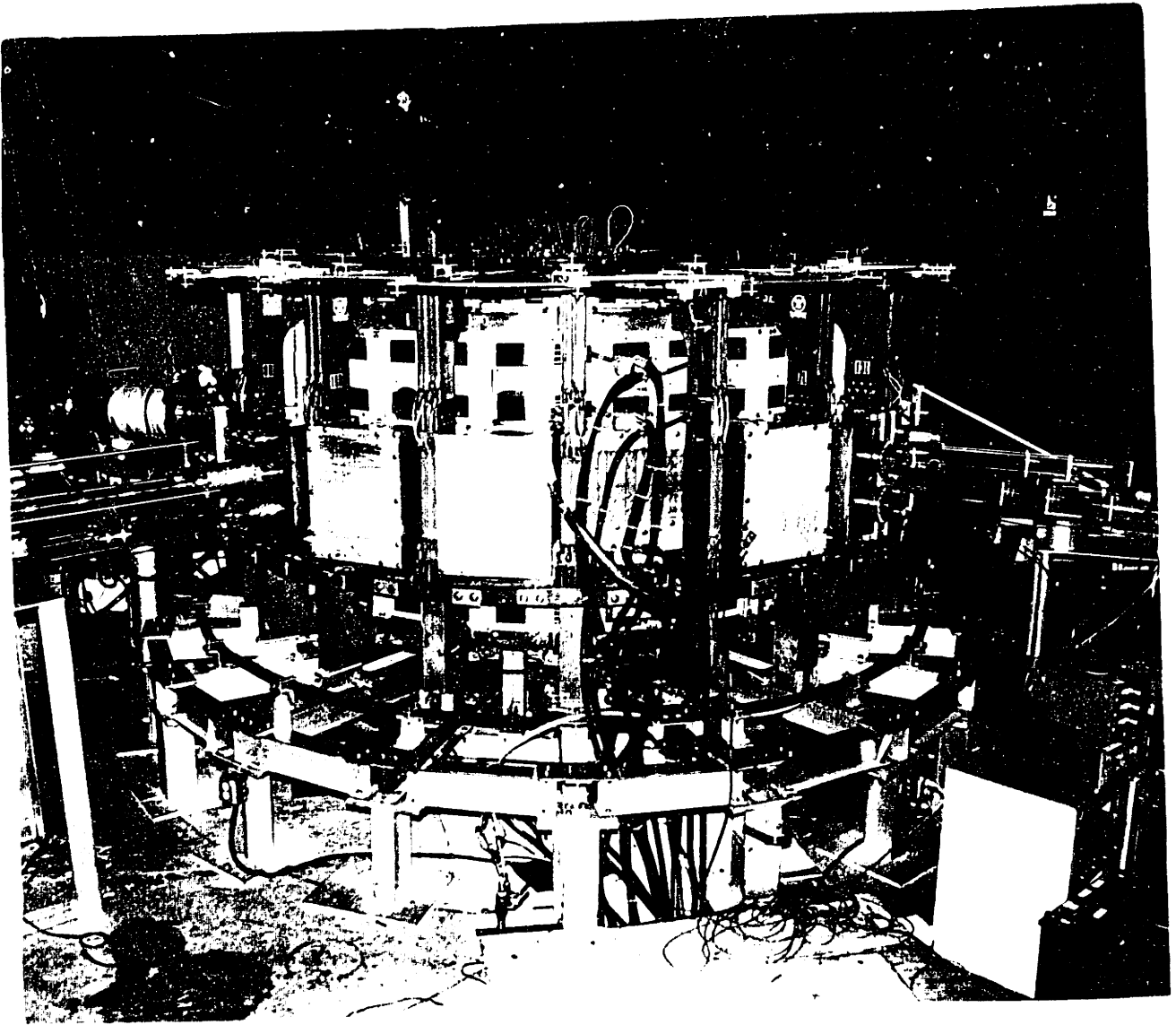
Figure 1-1: The Versatile Toroidal Facility.
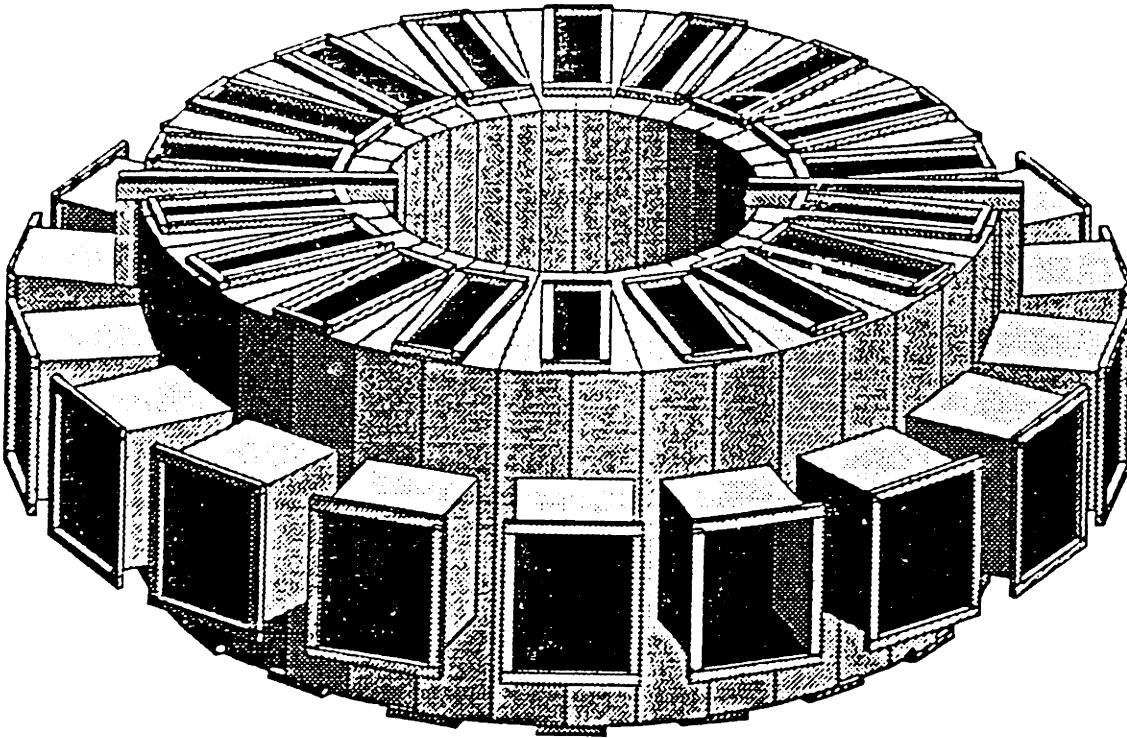
Figure 1-2: Diagram of the VTF vacuum chamber.

it slightly larger than Alcator C-MOD. The VTF chamber is equipped with 48 ports for installation of diagnostic equipment and power injection. The ports on the upper and lower faces of the chamber are only as deep as the chamber wall. The side openings protrude outward as box ports, with a depth of 50.2 cm.

The chamber is evacuated by a turbo molecular pump system designed by Dexter Beals, now a graduate student in electrical engineering at the VTF group. The pumping station is installed on one of the side ports. Ion gauges read the pressure at various points

along the pumping line as well as in the chamber. When pumped down, the chamber

generally reaches a pressure between 5×10^{-7} and 2×10^{-6} torr, depending on the levels

and outgassing rates of impurities in the chamber.

1.2 Plasma Configuration

The Oak Ridge magnets ("TF coils") surround the vacuum chamber, setting up a toroidal

field. In addition, there are several current-carrying cables which surround the entire

chamber, setting up a weak vertical field. This magnetic configuration, consisteing of

a strong toroidal field and a weak vertical field, is known as a HELIMAK confinement

scheme.

A microwave source injects 3 kW of 2.45 GHz radiation into one of the side ports,

producing electron-cyclotron resonance heating (ECRH) in the plasma. For the experi-

ments described in this thesis, the microwaves are the only source of plasma heating. For

these experiments, the toroidal field B_0 is set to 700 gauss. The vertical field B_v can be

varied from 0 to 20 gauss, changing the confinement characteristics of the plasma. For

most of the experiments, the vertical field was set at 10 gauss.

Although both hydrogen and argon plasmas have been produced in the VTF, all

experiments described here were conducted on hydrogen plasmas. To run the machine,

the chamber was filled with hydrogen to a total pressure of around 2.5×10^{-5} torr, keeping

the partial pressures of impurities under 10%. For each shot, the magnet power is turned

on, followed three seconds later by the microwave power. After sustaining a plasma for

eight seconds, the power systems shut off.

The configuration produces a plasma with an electron temperature around 10 eV and a density which varies spatially, but peaks at around 2×10^{10} cm^{-3}. The density profile is toroidally symmetric. Along the radial axis, it is peaked, at a radius which varies according to the vertical field. As B_v increases from zero to 10 G, the density peak becomes more pronounced and moves inward toward the center of the chamber. When B_v is increased to 20 G, the density peak becomes broader, but moves farther toward the center of the chamber. The density has been measured across the chamber (at the mid-plane) by sweeping a Langmuir probe during a shot. Figure 1-3 shows three density profiles taken during shots with different magnetic field strengths.
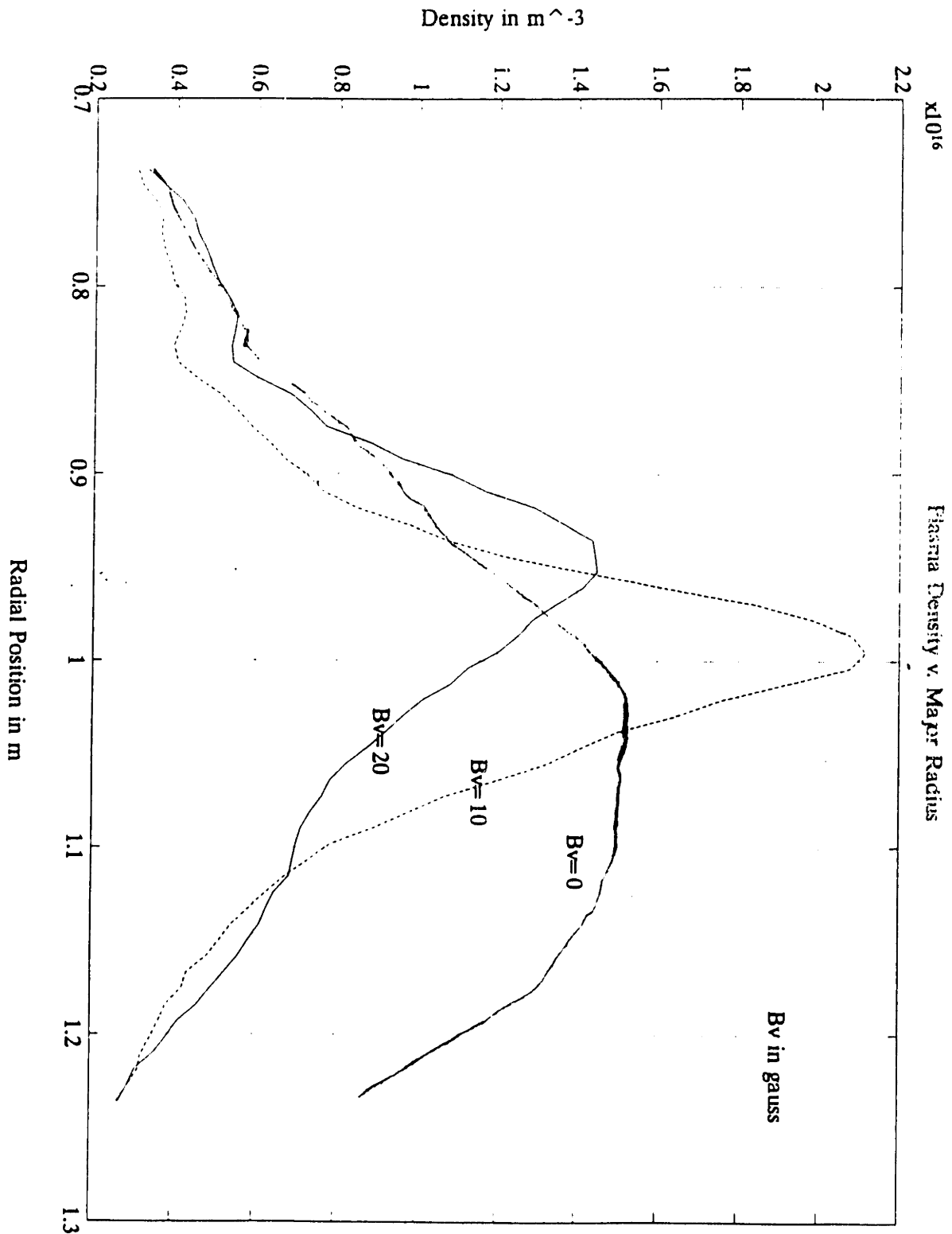
Figure 1-3: Midplane plasma density profiles for different vertical field strengths. Source: J. C. Rost, S. C. Luckhardt, R. R. Parker, E. D. Zimmerman, *Density and Potential Fluctuation Measurements in a Toroidal ECRH Sustained Plasma,* poster, APS Plasma Physics Meeting, Seattle, November 1992

18

Chapter 2

Background

2.1 Plasma Fluctuations.

Extensive theoretical and experimental work has been published which predicts conditions for turbulence in Helimak and TOKAMAK edge plasmas, but little work has been done as yet on HELIMAK plasmas of the type studied here. The main purpose of this thesis is to characterize some aspects of turbulence and potential fluctuations in the HELIMAK plasma.

From basic thermodynamics, we can see in a primitive way that some form of turbulence is to be expected. The confinement of the plasma by the external magnetic fields results in a density gradient in the plasma. This is a thermodynamically unstable situation, and creates free energy which can drive turbulent fluctuations.

Fluctuations in the VTF plasma are primarily measureable in the directions perpendicular to the magnetic field lines, which are primarily in the toroidal direction. The plasma tend᠊ to stream quickly along the field lines, causing any toroidal variation in the characteristics of the plasma to occur over a long distance scale. There is much

less large-scale movement of mass across the field lines, so spatial variations are more pronounced over distances significantly smaller than the size of the plasma chamber.

Measurements of radial potential fluctuations have been carried out on the VTF plasma by J. C. Rost, a graduate student at the VTF group, and the author. The data gathered indicated the presence of wave activity and turbulence in the radial direction in the chamber. Radial fluctuations have a correlation length of approximately 7 cm at most frequencies measured. [1].

2.2 Individual particle behavior: Cyclotron motion and E × B drift.

This section describes some of the particle motions which are relevant to an understanding of the HELIMAK plasma.

Plasma particles in constant electric and magnetic fields obey the basic electromagnetic equation of motion:

$$m\ddot{\mathbf{x}} = Q(\mathbf{E} + \frac{\dot{\mathbf{x}}}{c} \times \mathbf{B})$$ (2.1)

where all variables are in Gaussian (cgs) units.

The basic motion of a charged particle moving perpendicular to a uniform magnetic field, with zero electric field, is circular. The frequency ω_c of the oscillation, known as the cyclotron frequency, is independent of the particle's energy:

$$\omega_c = \frac{|Q|B}{mc}$$ (2.2)

[1]J. C. Rost, S. C. Luckhardt, R. R. Parker, E. D. Zimmerman, *Density and Potential Fluctuation Measurements in a Toroidal ECRH Plasma*, Poster, APS Plasma Physics Meeting, Seattle, November 1992.

20

The particle may also have a velocity parallel to the magnetic field, which is unaffected by the magnetic field. Thus the most general path is a helix. The motion in the plane perpendicular to **B** is a circle centered around a guiding center (x_{gc}, y_{gc}). Setting

$$\mathbf{B} = B\hat{z}$$

the perpendicular components of the particle's position become

$$x - x_{gc} = r_G \sin \omega_c t \tag{2.3}$$

$$y - y_{gc} = \pm r_G \cos \omega_c t \tag{2.4}$$

where r_G is the *gyro radius* of the orbit[2],

$$r_G = \frac{(v^2 - v_z^2)^{\frac{1}{2}}}{\omega_c} \tag{2.5}$$

or, in terms of the particle's kinetic energy T,

$$r_G = \frac{(\frac{2T}{m} - v_z^2)^{\frac{1}{2}}}{\omega_c} \tag{2.6}$$

Adding a constant electric field (for simplicity's sake, in the x-z plane), the equation of motion in the $\hat{z}$ direction (the $\hat{z}$-component of Equation 2.1) becomes:

$$\ddot{z} = \frac{Q}{m} E_z \tag{2.7}$$

which is merely a constant acceleration. If, however, collisions are taken into account for motion parallel to **B**, then the $\hat{z}$-direction motion becomes a steady drift (for sufficiently small E_z). This effect results in a non-zero electrical resistivity in the plasma.

---

[2]The $\pm$ in Equation 2.4 results from the division of $|Q|$ by Q in the derivation of the equation. Its physical significance is that positive and negative particles orbit in opposite directions.

Perpendicular to B, the equations of motion must include a magnetic term:

$$\ddot{x} = \frac{Q}{m} E_x \pm \omega_c \dot{y} \tag{2.8}$$

$$\ddot{y} = \mp \omega_c \dot{x} \tag{2.9}$$

These coupled differential equations can be uncoupled by taking another time derivative:

$$\dddot{x} = \pm \omega_c \ddot{y} = \pm \omega_c (\mp \omega_c \dot{x}) \tag{2.10}$$

$$\dddot{y} = \mp \omega_c \ddot{x} = \mp \omega_c (\frac{Q}{m} E_x \pm \omega_c \dot{y}) \tag{2.11}$$

Using Equation 2.2, Equation 2.11 becomes:

$$\dddot{y} = \mp \frac{|Q|B}{mc} \frac{Q}{M} E_x \mp (\pm \omega_c^2 \dot{y}) \tag{2.12}$$

$$Q = \pm |Q| \implies \dddot{y} = -\omega_c^2 (\frac{E_x}{B} c + \dot{y}) \tag{2.13}$$

It is useful to make the substitution

$$y' \equiv y + \frac{E_x}{B} ct \tag{2.14}$$

and transform Equation 2.13 into

$$\dddot{y}' = -\omega_c^2 \dot{y}' \tag{2.15}$$

The equations of motion are now those for unperturbed cyclotron motion in x, y'. In other words, the particle undergoes cyclotron gyration at ω_c about a guiding center drifting at speed

$$\mathbf{v}_{gc} = \frac{E_x}{B} c\hat{\mathbf{y}} \tag{2.16}$$

We can generalize this result to coordinate systems where $\mathbf{B}$ does not lie along the $\hat{z}$ axis and $E_y \neq 0$ by noting that, in the original coordinates,

$$\frac{E_x}{B} = \frac{|\mathbf{E} \times \mathbf{B}|}{B^2} \tag{2.17}$$

and

$$(\mathbf{E} \times \mathbf{B}) \| \hat{y} \tag{2.18}$$

Making these substitutions, we can restate Equation 2.16 as

$$\mathbf{v}_{gc} = \frac{c}{B^2} \mathbf{E} \times \mathbf{B} \tag{2.19}$$

which is independent of coordinate system.

There are several surprising aspects of this result. First it is not only independent of Q and m, but also of the *sign* of Q: Ions and electrons drift in the same direction at the same speed. In a plasma, this motion manifests itself macroscopically as a flow of neutral mass in the direction perpendicular to both $\mathbf{E}$ and $\mathbf{B}$. The phenomenon is known as $\mathbf{E} \times \mathbf{B}$ *drift*.

Chapter 3

Experimental Apparatus

The experiments described herein were conducted using an array of Langmuir probes designed by the author during the summer of 1991, constructed between August 1991 and June 1992, and tested and installed in September 1992. As shown in Fig. 3-1, The device consists of eight probes arranged in a linear array 8.53 cm long. Each probe is a stainless steel wire 0.89 mm in diameter, with an exposed length of 6mm. The potential of each probe relative to the grounded vacuum chamber was measured by sending the signal through an RF filter to an isolation amplifier circuit. The amplifier output was sent to a low-pass filter, the output of which was digitized by the VTF's CAMAC data acquisition system. The circuit and data acquisition system can handle four channels of data simultaneously, digitizing at a 40 kHz data rate for 0.82 seconds. This permitted measurement of the floating potential of the plasma at up to four different probes (and hence four vertical positions) during a single shot.

3.1 The VTF Probe Array

3.1.1 Internal Structure

The vertical probe array is designed around a "backbone," a pipe of type 304 stainless steel, part of which is shown as part A in Fig. 3-1. The pipe is 40.4 inches long, with an outer diameter of 1" and a wall thickness of 0.125". Coaxial cables which carry the probe signals run through this pipe. In addition, the pipe serves as a cantilever to support the probe array inside the vacuum chamber. Its back end is welded to the inside of a ring with an inner diameter of 1" (to fit the pipe snugly) and an outer diameter of 1.37". The outside of the ring is welded to the inside of a double-sided high-vacuum flange with an outer diameter of 2.75" (Part B in Fig. 3-1). Because both faces of the ring are under vacuum, several ventilation holes were drilled through it to permit the rear of the system to be pumped out. The ring was machined by Randolph West and Kevin Walsh, and was welded by Christopher Shutts. All three are students at the VTF group. The pipe was electro-polished at Arborway Metal Finishing, Inc., in Dorchester, Mass.

3.1.2 Probe Support Structure

The forward end of the pipe is cantilevered into the vacuum chamber. Its end is bolted to two brackets (Fig. 3-2, part A) which hold a support bar in place. This first support bar (Fig. 3-2, part B), a piece of stainless steel $\frac{1}{2}$" $\times$ $\frac{1}{2}$" $\times$ $5\frac{1}{2}$", holds the forward ends of the signal cables. These lines are semi-rigid coaxial cables, with a core conductor of copper, a stainless steel shield, and a Teflon dielectric. The outer diameter of the cable

VTF VERTICAL PROBE ARRAY

PROBE CROSS-SECTION:

ceramic sheath
grounded shield
inner ceramic sheath
probe wire

signal feedthroughs

welded bellows

B

semi-rigid coaxial cable
(extends to feedthroughs)

A

side port

toroidal chamber

plasma

26
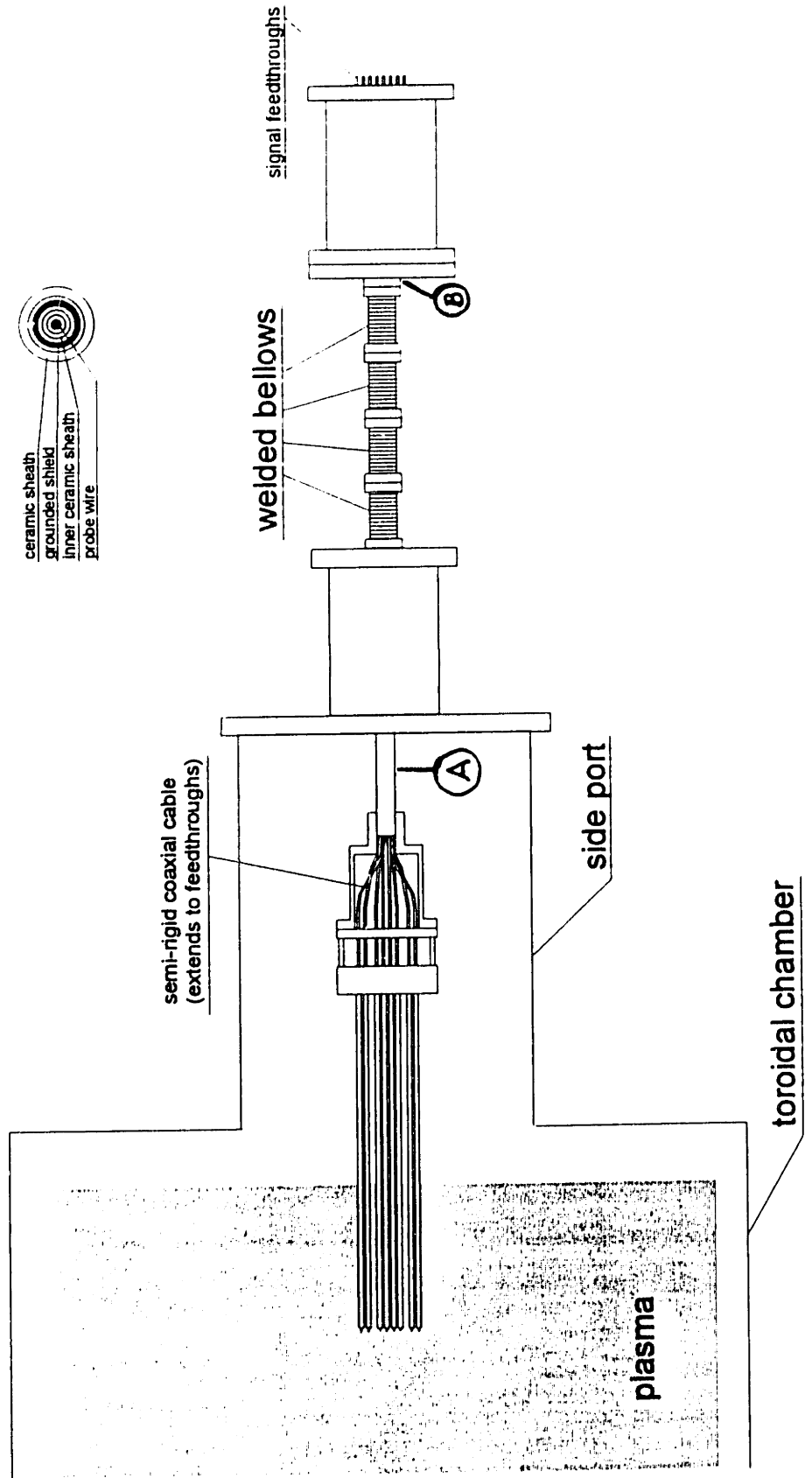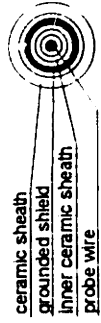
Figure 3-1: Schematic diagram of VTF probe array.
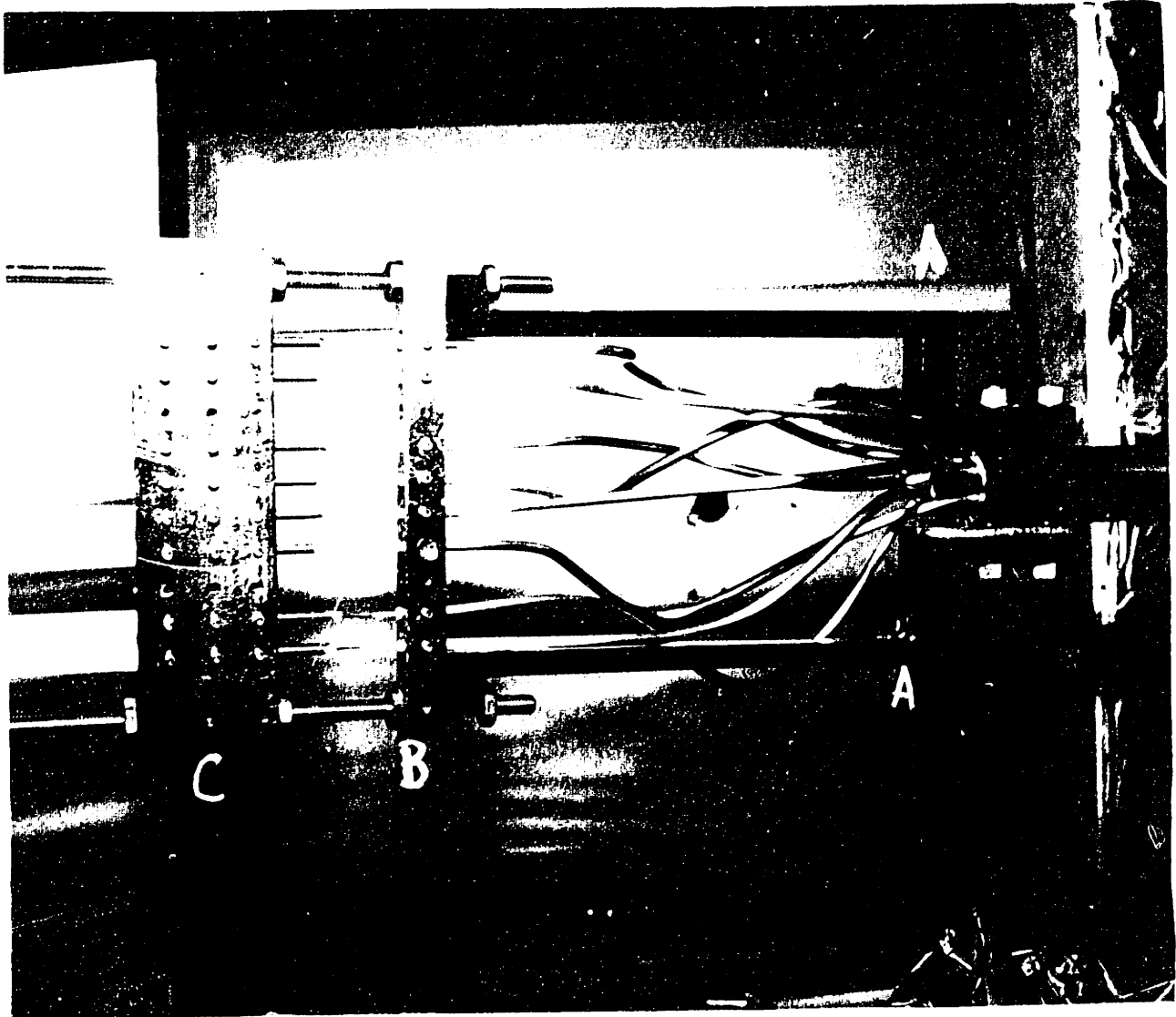
Figure 3-2: Probe support structure. A: Brackets. B: Coax support bar. C:Probe support bar.

is 0.141". Each cable runs through a 0.145" hole in the support bar, and is held in place by a set screw (tap size 5-40). This junction makes electrical contact with the shield, keeping it grounded to the chamber wall. The support bar was machined by Randolph West.

The first bar is bolted to threaded rods which extend past it, and are attached to a second support bar (Fig. 3-2, part C), which holds the probes and their shields in place. The second bar, diagrammed in Fig. 3-3, was machined to 0.001" tolerances (to keep the probes parallel) by Peter Dandridge, Jr. at Atomic, Ltd., in Cambridge, Mass.

The stainless steel probe wires are soldered to the center conductor of the coaxial cables in the space between the two support bars. The connection was made with vacuum-grade Welco #5 tin-silver solder. A ceramic (alumina) tube of inner diameter 0.047", outer diameter 0.078" and length 22" surrounds each probe wire. It terminates approximately $\frac{1}{2}$" behind the back of the second support bar. Outside the spacer is a stainless steel shield with an outer diameter of 0.12" and an inner diameter of 0.09". Its rear end is crimped, holding the ceramic spacer in place and preventing it from sliding. This shield fits snugly in the narrow section of the second support bar, where it is held in place by a set screw. This provides an electrical connection, keeping the shield grounded to the chamber wall. Outside the shield, the grounded metal and the plasma are separated by another ceramic shroud. This tube has an outer diameter of 0.250" and an inner diameter of 0.175", with a length of 21". It terminates one inch inside the second support, where the 0.260" hole tapers to 0.125". Within the 0.260" hole, the tube

FORWARD VIEW

SIDE VIEW

6-40
TAP
(30 HOLES)

0.250"   1.00"   0.250"   0.375"   0.125"   0.250"   1.50"   5.50"

REAR VIEW

0.250"   0.125"   0.250"   0.50"
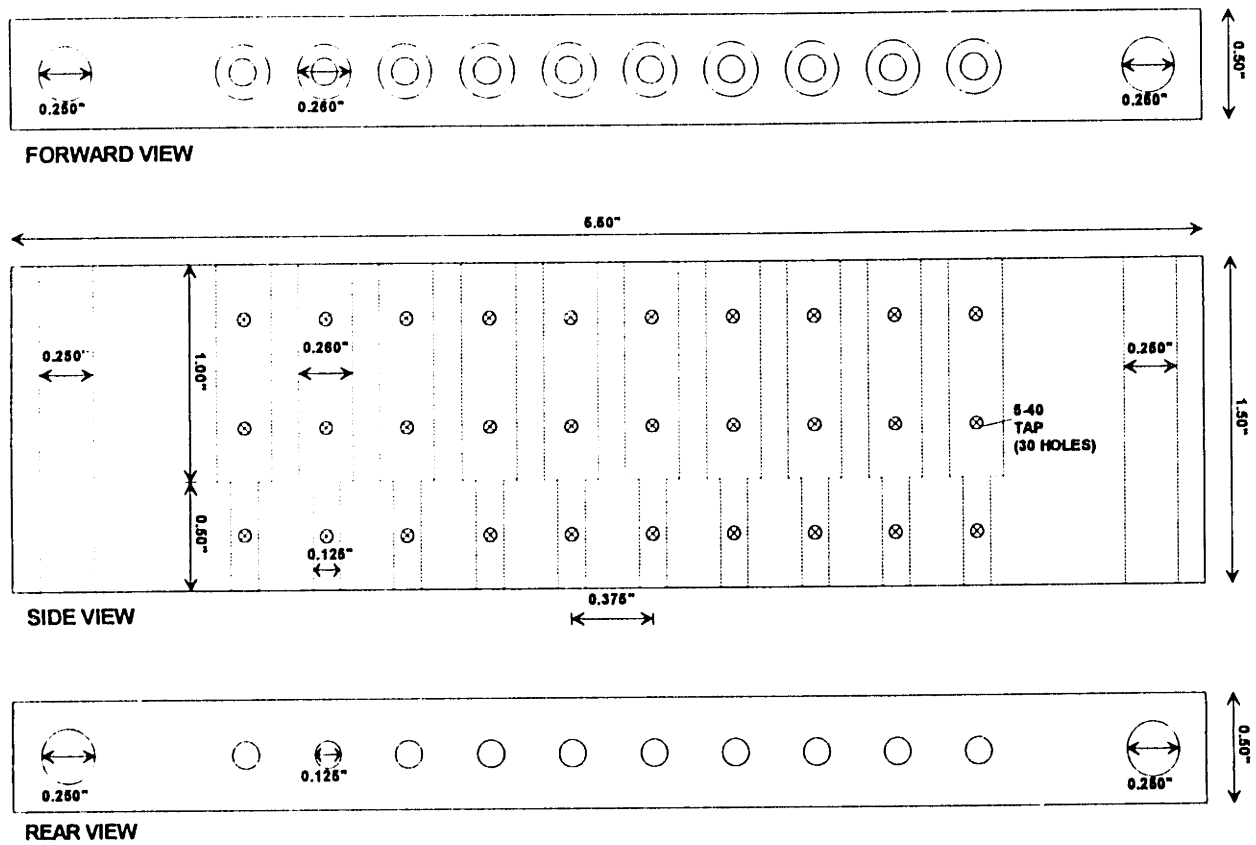
Figure 3-3: Schematic diagram of second support bar

29

PROBE	POSITION (± 0.05 cm)
1	4.27
2	3.40
4	1.47
5	0.71
6	-0.41
7	-1.50
9	-3.38
10	-4.27

Table 3.1: Measured probe locations relative to center of array, which is aligned at the mid-plane of the VTF vacuum chamber. All dimensions in centimeters.

is held in place by two set screws. Its forward end is closed, except for a 0.045" hole, through which the probe wire extends approximately $\frac{1}{4}$". The spacer tube and ground shield terminate immediately inside the closed end of the outer shroud. The probe tips are shown in Fig. 3-4. Although the support brackets are designed to accomodate ten probes, only eight are installed, leaving the third position from each end blank. The probes are numbered, however, according to their position, from top to bottom: 1, 2, 4, 5, 6, 7, 9, and 10.

Because the ceramic sheaths are not perfectly straight, there is some variation between the theoretical and actual probe spacings. The measured locations of each probe along the vertical axis are presented in Table 3.1.

3.1.3 Bellows Assemblies

At the rear end of the main pipe, the forward face of the double-sided vacuum flange is bolted to the first of a series of four welded bellows assemblies, which permit the pipe
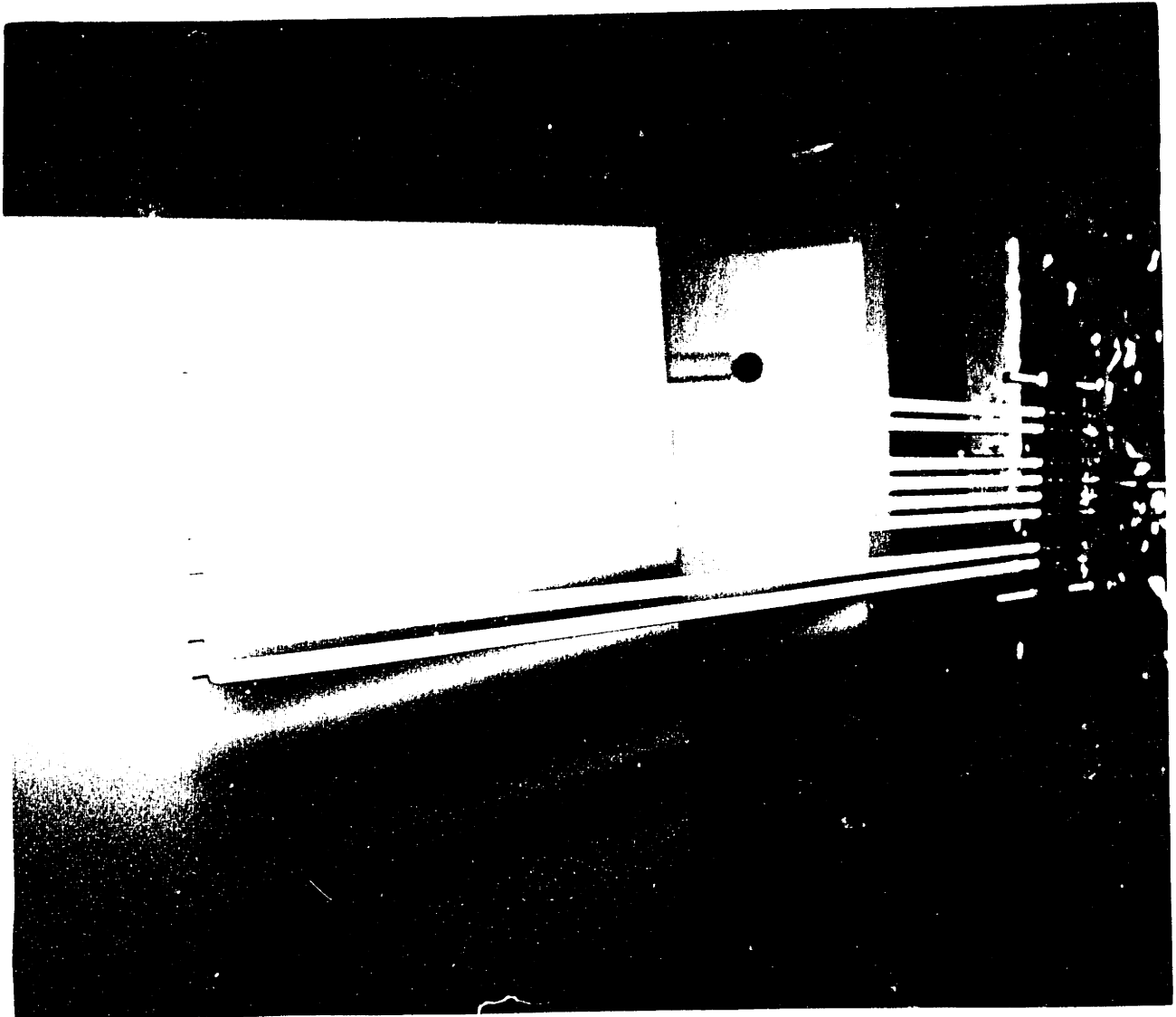
Figure 3-4: Photograph of probe tips.

(and hence the probe array) to be moved to different radial positions. All of the bellows, purchased from Huntington Laboratories, are 0.007"-wall type 316 stainless steel, and have an inner diameter of 1.04", enabling the pipe to slide through them.

The first (Part A, Fig. 3-5) and fourth bellows are identical, with a compressed length of 0.92" and a stroke of 5.70". Each of these bellows is welded to a $3\frac{3}{8}$" flange on one end and a half-nipple with a $2\frac{3}{4}$" flange on the other. A support ring with ventilation holes and an inner diameter of 1.02" was welded inside the half-nipple of the fourth bellows, so that the bellows are supported on the pipe at the ring, and the compressible sections do not drag along the surface of the metal.

The second and third bellows each have a compressed length of 0.87" and a stroke of 4.50". They are welded to $3\frac{3}{8}$" flanges at either end. All four flange-to-bellows connections were initially machined and arc-welded by Peter Dandridge Sr. at Atomic, Ltd. The second bellows (Fig. 3-6) was later replaced due to a manufacturing defect. Electron-beam welding on the replacement was performed at Applied Energy, Inc., in Winchester, Mass.

At each of the three junctions where one bellows assembly meets another, an extra $3\frac{3}{8}$" double-sided flange, a machined blank flange, is bolted between them. This flange has a 1.02" hole bored through its center, and several ventilation holes around it, and serves to support the bellows assemblies around the main pipe.

The bellows permit the probe tips to be moved to any major radius from 81.5 cm to 127.5 cm (1.5 cm inside the box port).
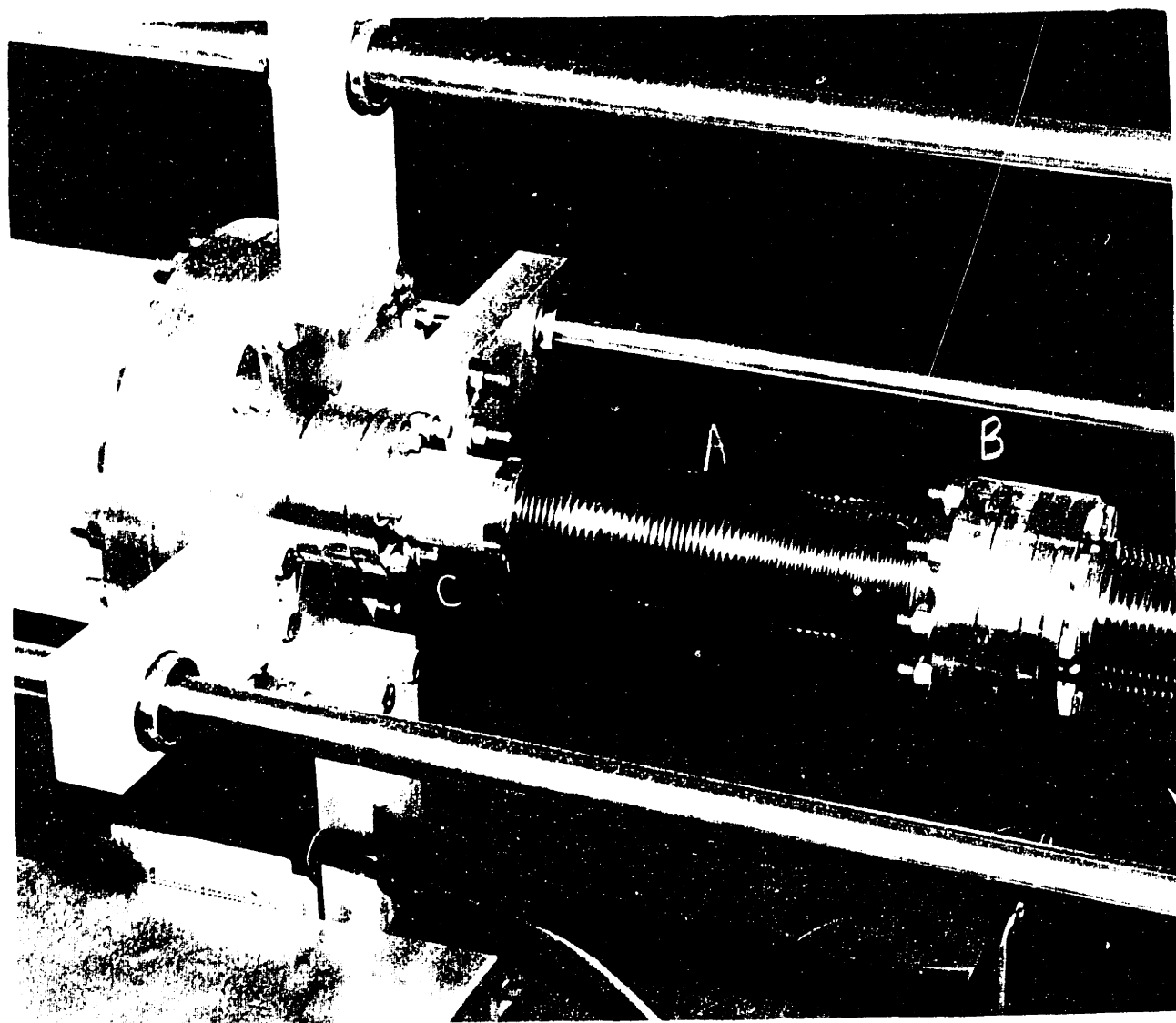
Figure 3-5: Bellows assembly #1. A: Welded bellows. B: $3\frac{3}{8}''$ flange. C: Half-nipple with $2\frac{3}{4}''$ flange.
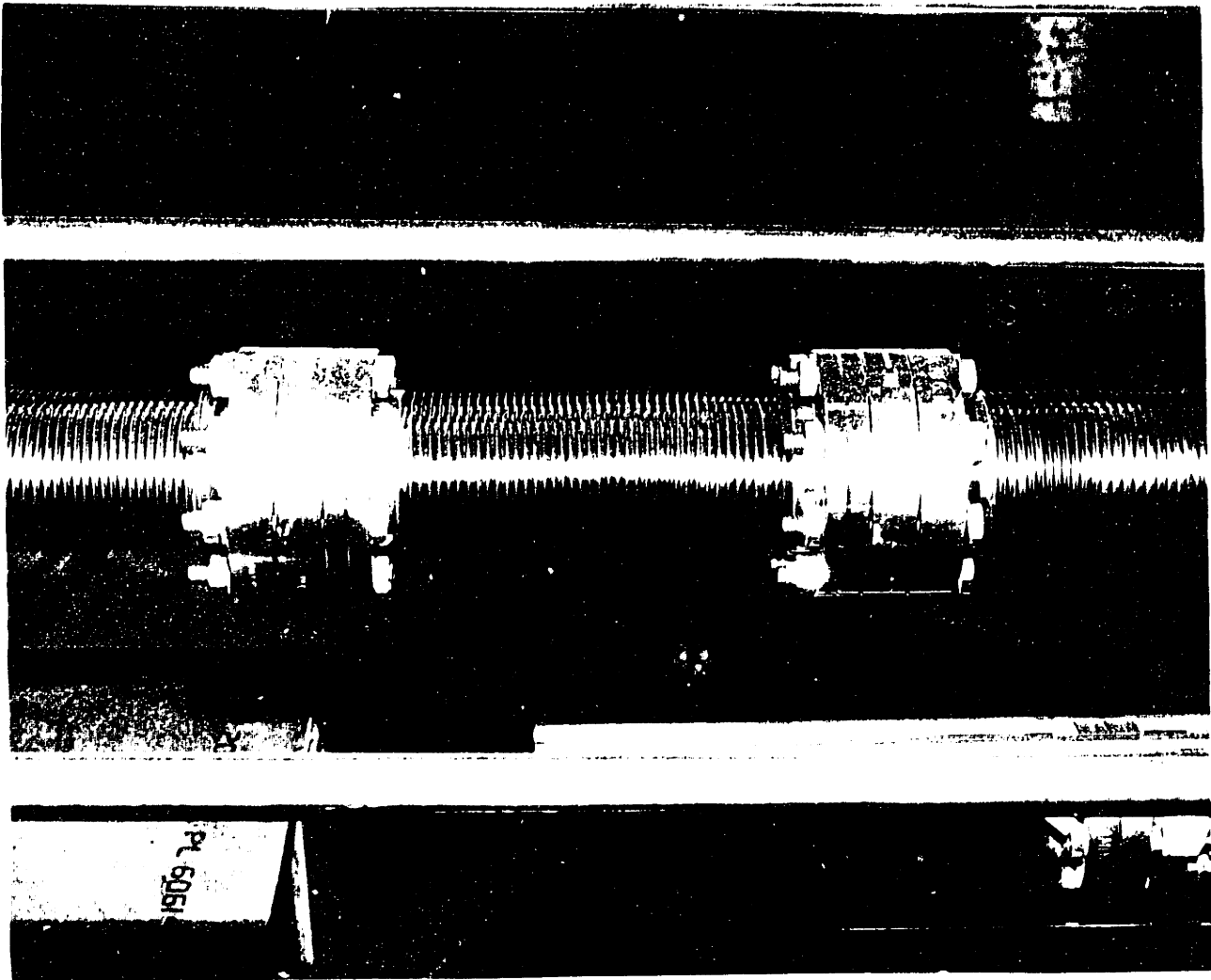
Figure 3-6: Bellows assembly #2.

3.1.4 Connection to the Vacuum Chamber

The $2\frac{3}{4}$" flange on the fourth bellows is bolted to a "zero-length" adapter flange, which mounts to an 8" flange on the forward side. It is bolted to a half-nipple with a rotatable flange. The pipe of the half-nipple is welded to a port cover which seals one of the tangential ports of the VTF chamber. The port cover, machined at Atomic, Ltd., seals to the chamber with a rectangular O-ring. The weld between the half-nipple and the port cover, besides providing a vacuum seal, acts as the forward support for the weight of the probe structure.

3.1.5 Signal Feedthroughs and External Structure

At the rear of the structure, the pipe flange is bolted to a zero-length adapter flange with an 8" diameter. The coaxial cables extend through the flange into an 8" nipple, where they terminate in BNC connectors. These connectors are attached by Welco tin-silver solder.

Attached to the bolt-holes of each flange of the nipple are three "ears," pieces by which the apparatus is suspended from stainless steel rails. Each rail runs through a support bushing in the ear, enabling the nipple, rigidly connected to the probe array, to slide along the rails, which terminate in a support piece which rests on a table.

The back plate of the apparatus is an 8" blank flange which is bolted to the nipple. Into the flange are welded eight double-ended BNC signal feedthroughs. This piece was machined and welded by Peter Dandridge Sr., at Atomic Ltd. The coaxial cables are

connected to the inside end of the feedthroughs, and the signal is sent to the air side of the flange.

3.2   Amplifier Circuit

The vertical probe array has a set of amplifier circuits dedicated to it. The circuit setup was built primarily by Jenise Bushman, a student in the VTF group. It has four independent signal channels, each consisting of an operational amplifier circuit whose output runs to an isolation amplifier. The output of the isolation amplifier is sent to a low-pass filter, from which the signal enters the data acquisiton system.

3.2.1   Circuit Components

The complete circuit diagram is shown as Fig. 3-7. The circuit is housed in an aluminum chassis, 11" × 17" × 2".

A BNC cable is connected to the feed-through on the back plate of the probe apparatus. The signal goes through a 9 MHz low-pass filter (Mini-Circuits model BLP-5), which is contained in a small cylinder with a BNC connector on either end. The filter's purpose is to block any microwave signals the probe may have picked up from the ECRH wave. The plug on the end of the filter is connected to a BNC jack on the front panel of the circuit chassis.

The input signal, relative to the machine ground (cable shield), is initially sent through a buffer amplifier. This consists of an operational amplifier (an OP07 precision op-amp) wired as an inverting amplifier. This buffer amplifier sets the gain of the circuit
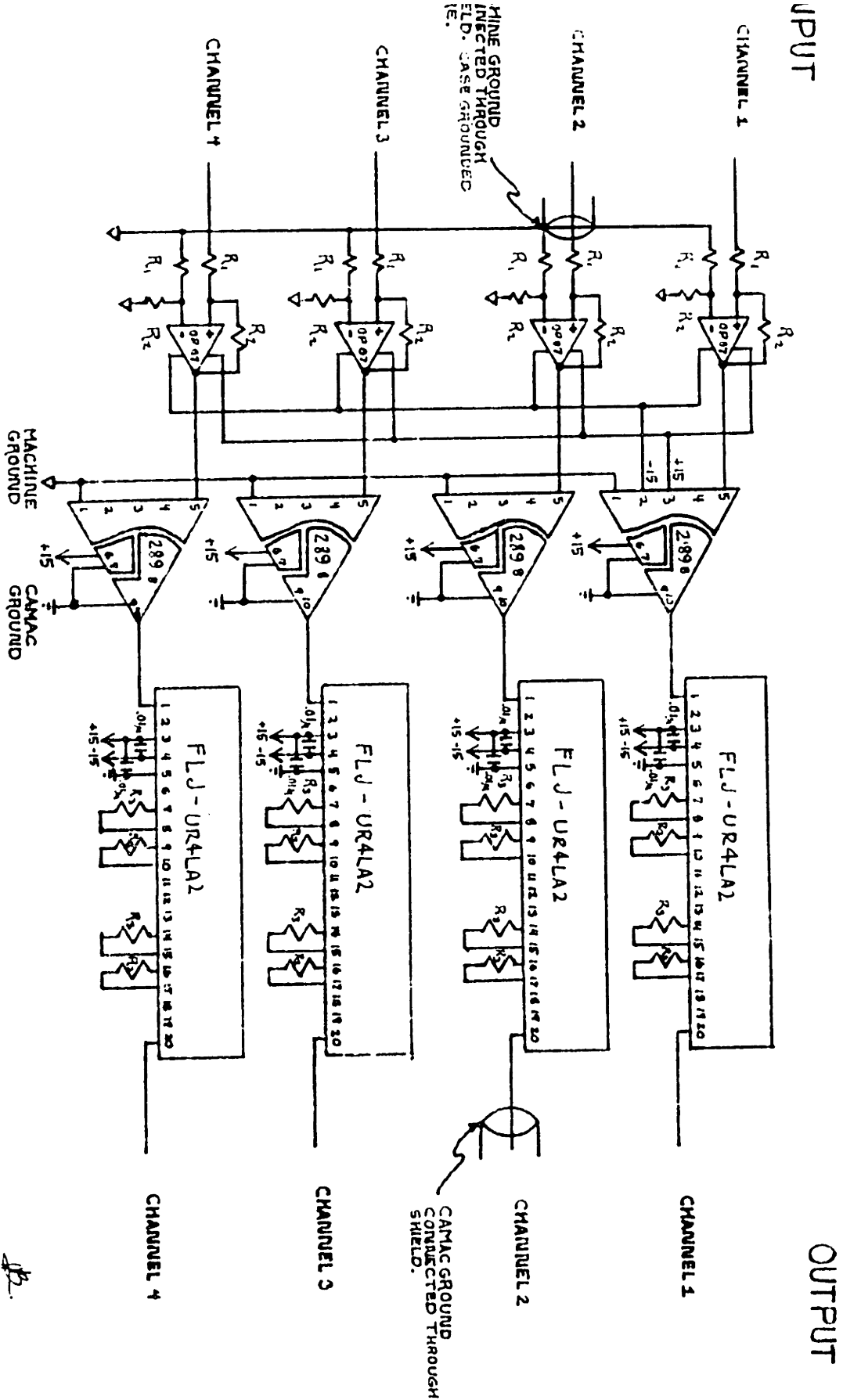
Figure 3-7: Diagram of amplifier circuits.

(unity in these experiments). In addition, the op-amp acts as a fuse, protecting the data acquisition system from any high-voltage pulses which might result from a catastrophic plasma collapse.

The output of the buffer amplifier and the machine ground are connected to the inputs of an Analog Devices isolation amplifier, model 289L. This integrated circuit provides total electrical isolation between the CAMAC system ground and the machine ground, as well as between the CAMAC and the input signal. The amplifier has a specified bandwidth of 20 kHz, above which it attenuates by 24 db/oct. Testing has determined that the frequency response begins to drop below unity at approximately 17 kHz.

The output signal from the isolation amplifier and the CAMAC ground signal are connected to the input and ground terminals of a low-pass filter circuit. The filter is an integrated circuit, DATEL model FLJ-UR4LA2. It is used to cut out signals above 20 kHz, to prevent higher frequency components from entering the digitizing equipment and aliasing to spurious signals.

3.2.2   Signal Grounds

The probe circuit maintains complete electrical isolation between the CAMAC and the vacuum chamber. The chassis is grounded to the machine through the shield of the BNC connector on channel 2. The CAMAC ground enters the chassis through an isolated double-ended Lemo connector on the output of channel 2, and is connected to the second conductor of each of the other outputs.

Chapter 4

Single-Point Measurements

This chapter presents plasma potential time series data obtained from individual probes, as well as spectral analysis of these data.

4.1 Fluctuation Amplitudes

The first aspect to be addressed in the study of plasma fluctuations is their amplitude, defined in this case to be the standard deviation $\Delta\phi$ of the floating potential:

$$\Delta\phi = \sqrt{\langle\phi^2\rangle - \langle\phi\rangle^2} \qquad (4.1)$$

where $\langle\ \rangle$ indicates a time averaged (expectation) value.

The fluctuation amplitudes of the measured potentials were obtained by calculating the standard deviation of time series electrostatic potential data over 0.82-second digitizing periods during shots. The fluctuation amplitude was found to be essentially independent of probe number (i. e. constant over the length of the probe array), but strongly dependent on radial position. This suggests that the fluctuations are indeed a result of the radial density gradient, as predicted. Table 4.1 shows the relation between

39

R (cm)	n (± 0.2) $\times 10^{10}$ cm^{-3}	$\Delta\phi$ (± 0.01) V
84	0.4	0.179
94	1.2	0.196
105	1.3	0.682
117	0.5	1.030

Table 4.1: Measured fluctuation amplitude $\Delta\phi$ as a function of major radius R and plasma density n.

major radius R, approximate plasma density n, and measured fluctuation amplitude $\Delta\phi$. The largest fluctuation amplitudes occur at locations where the density gradient is negative, i. e. on the outer slope of the density peak.

4.2 Frequency Spectra

This section presents time series fluctuation data analyzed using fast Fourier transform methods.

The time series signals obtained from the probe array were analyzed using MATLAB signal processing software to obtain Fourier transforms of the data. The power spectrum, defined as the squared magnitude $\tilde{x}(\omega)\tilde{x}^*(\omega)$ of a time function $x(t)$, indicates the level of fluctuation activity at a particular frequency.

The power spectra of the potential fluctuations measured exhibited strikingly different behavior in two different frequency ranges. At low frequencies (below 2 kHz), the spectrum is dependent on the radial position of the probes. At the innermost and outermost radii (117 and 84 cm), where the plasma density is low, the spectrum is fairly flat below 1 kHz. This is seen in Figures 4-1 and 4-4. At $R = 105$ cm, on the outer slope

of the density peak, the spectrum exhibits a broad peak around 500 Hz. This is seen most easily in the full log plot, Fig. 4-2. On the inner slope of the density peak, a similar but much smaller peak occurs at approximately 400 Hz (Fig. 4-3). The reasons for these broad spectral peaks are unknown.

Above a roll-off frequency (1 to 2 kHz, depending on radius), the power spectrum drops off according to a power law. Although the full log plots are not all perfectly linear in this frequency range, it is apparent that they all obey, at least approximately, the single-term power law:

$$\frac{\mathrm{d}\log y}{\mathrm{d}\log x} = g \tag{4.2}$$

where g is a constant. In the experimental data, g is always near 2; the power spectrum drops as $1/\omega^2$ in the high-frequency range.

Semi-logarithmic plots of the same frequency data are contained in Appendix A.

4.3 Time-Averaged Signals

The time-averaged potential was found to be nonzero in these experiments, and this value, the local floating potential, and its spatial structure are discussed here.

By averaging the signals from individual probes over three seconds of data digitized at 1 kHz, we obtain a measure of the plasma floating potential. The floating potential is a useful measurement: by sampling several probes at the same time, an approximate measure of the vertical electric field can be gathered. This, along with knowledge of the toroidal magnetic field, permits a calculation of the radial component of the plasma's
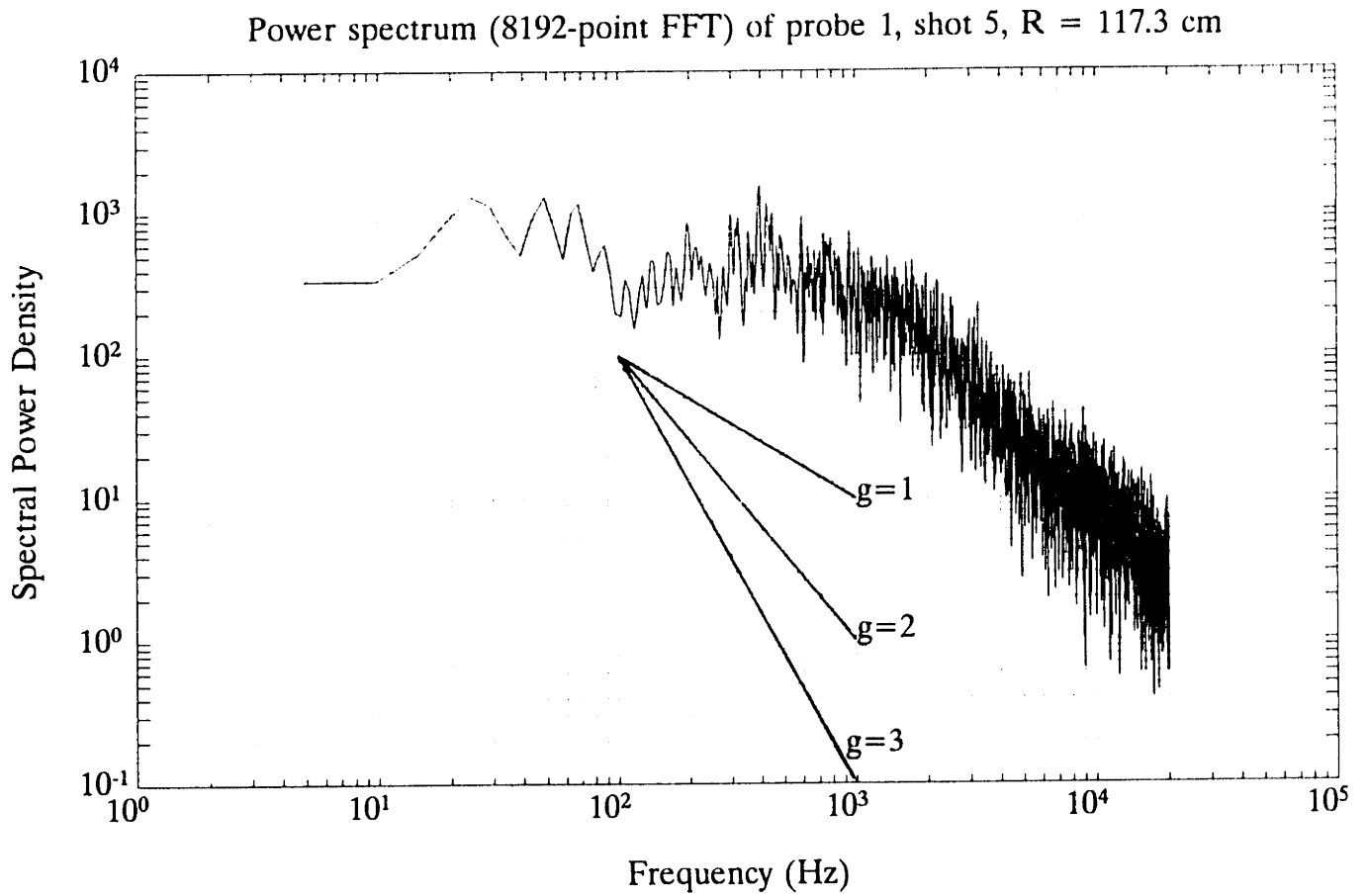
Figure 4-1: Full logarithmic plot of fluctuation power spectrum. Major radius 117.3 cm. Composite of four 8192-point FFTs. Lines are also shown indicating the slope corresponding to g=1,2,3.
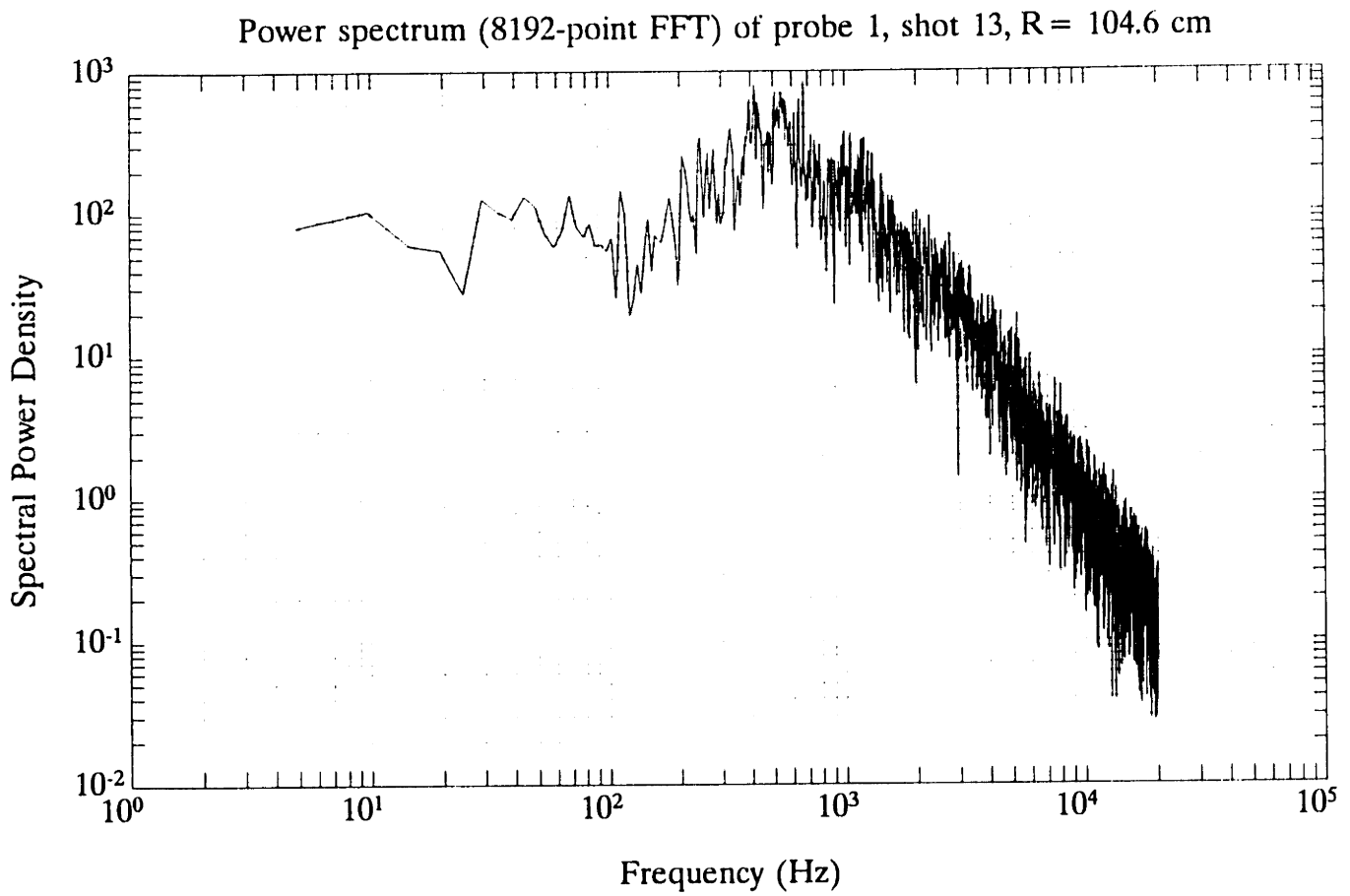
Figure 4-2: Full logarithmic plot of fluctuation power spectrum. Major radius 104.6 cm.

Power spectrum (8192-point FFT) of probe 1, shot 16, R = 94.4 cm
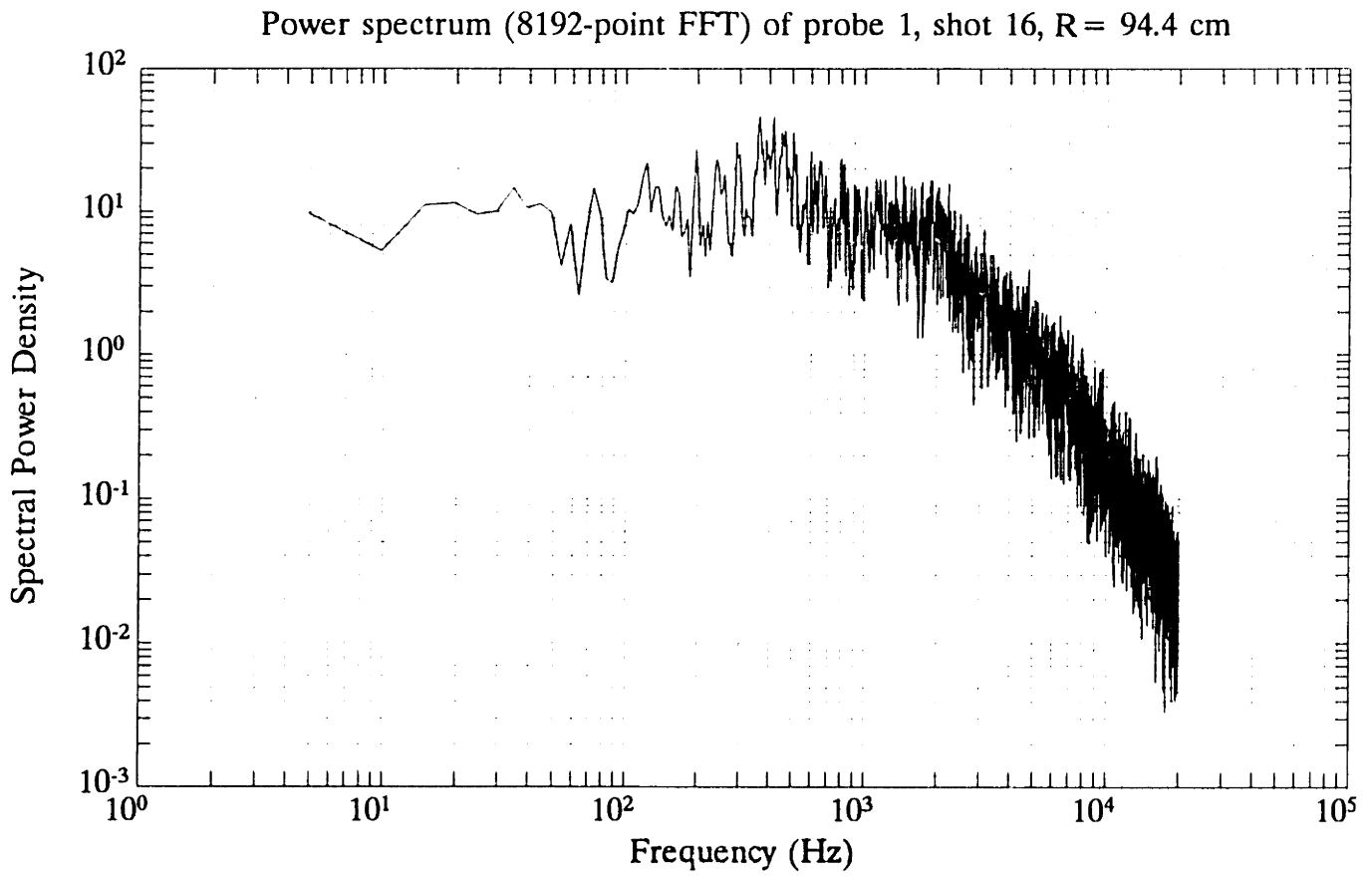
Figure 4-3: Full logarithmic plot of fluctuation power spectrum. Major radius 94.4 cm.
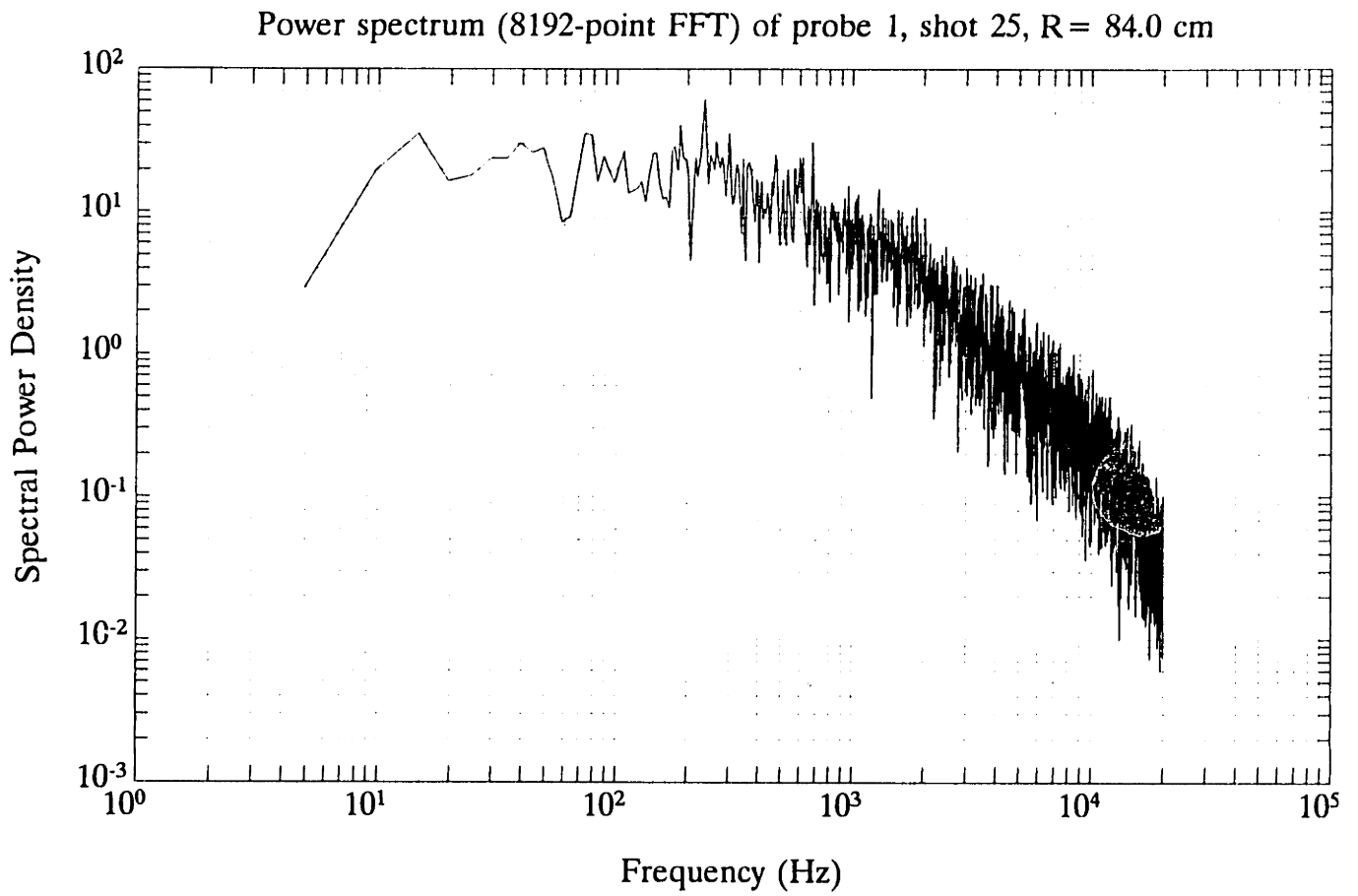
Power spectrum (8192-point FFT) of probe 1, shot 25, R= 84.0 cm

Figure 4-4: Full logarithmic plot of fluctuation power spectrum. Major radius 84.0 cm.

velocity caused by the $E \times B$ drift.

In all shots studied, the potential shows little or no sign of a trend over the duration of the samples; the time-averaged signal is stationary and thus a meaningful datum. This was determined by examining "running averages" of the potential data from a given probe over the duration of the digitizing. The running average splits the data set into a given number (in this case thirty) of consecutive segments, each covering an identical time period. The measurement is time-averaged over each of the segments, producing a thirty-point array. This was done for each data set analyzed, and none exhibited significantly more than small random variations over the duration of the data.

Due to the fact that the amplifier circuits can only handle four channels, it is not possible to obtain data for all eight probes simultaneously; several shots must be used. The plasma potential does not repeat its value exactly from shot to shot, although it is constant for the duration of any given shot. The floating potential as measured by the probes thus varies systematically and significantly from one shot to the next. However, the difference between the signals from a given pair of probes appears to vary less than the signals themselves. Thus a plot of the averaged potential versus probe position must include data from several shots, but the mean values of the potential do not constitute a measurement which is expected to be accurate for any given shot; this does not appear to be a measurement error.

In fact, the electric field "measurement" gained by averaging potential data from many shots may not even be accurate, as the errors can be very different during the

shots when different probes were sampled. This problem could be avoided completely by adding a second set of four amplifier channels in future experiments, permitting all probes to be monitored in a single shot. However, the cause of the shot-to-shot variation is not understood and further experiments will be needed to clarify this effect.

4.3.1 Data Normalization

An approach which appears to reduce significantly the "random" error under some circumstances is to determine the electric field by measuring the floating potential over many shots, and then subtract the measured potential at a fixed probe from all data. The efficacy of this type of normalization is demonstrated in Figures 4-5 and 4-6, where a set of data is shown before and after normalization.

After referencing the data to the signal from a particular probe, we are left with measurements of the relative potential at seven probes, while the potential of the eighth is defined to be zero— in effect, the loss of one data point is the price of the reduction of the shot-to-shot variation which appears to be inherent in the plasma. This does not translate into a loss of information about the electric field, because the field is independent of a uniform offset.

There are many possible explanations for the shot-to-shot variations which the plasma demonstrates. A possible source of this variation is the fact that the hydrogen fill pressure in the chamber was not well regulated, and varied by as much as 15% between shots.

Shot-to-shot variations only appear to be large enough for the normalization technique to significantly improve precision at the outermost radii of the chamber.
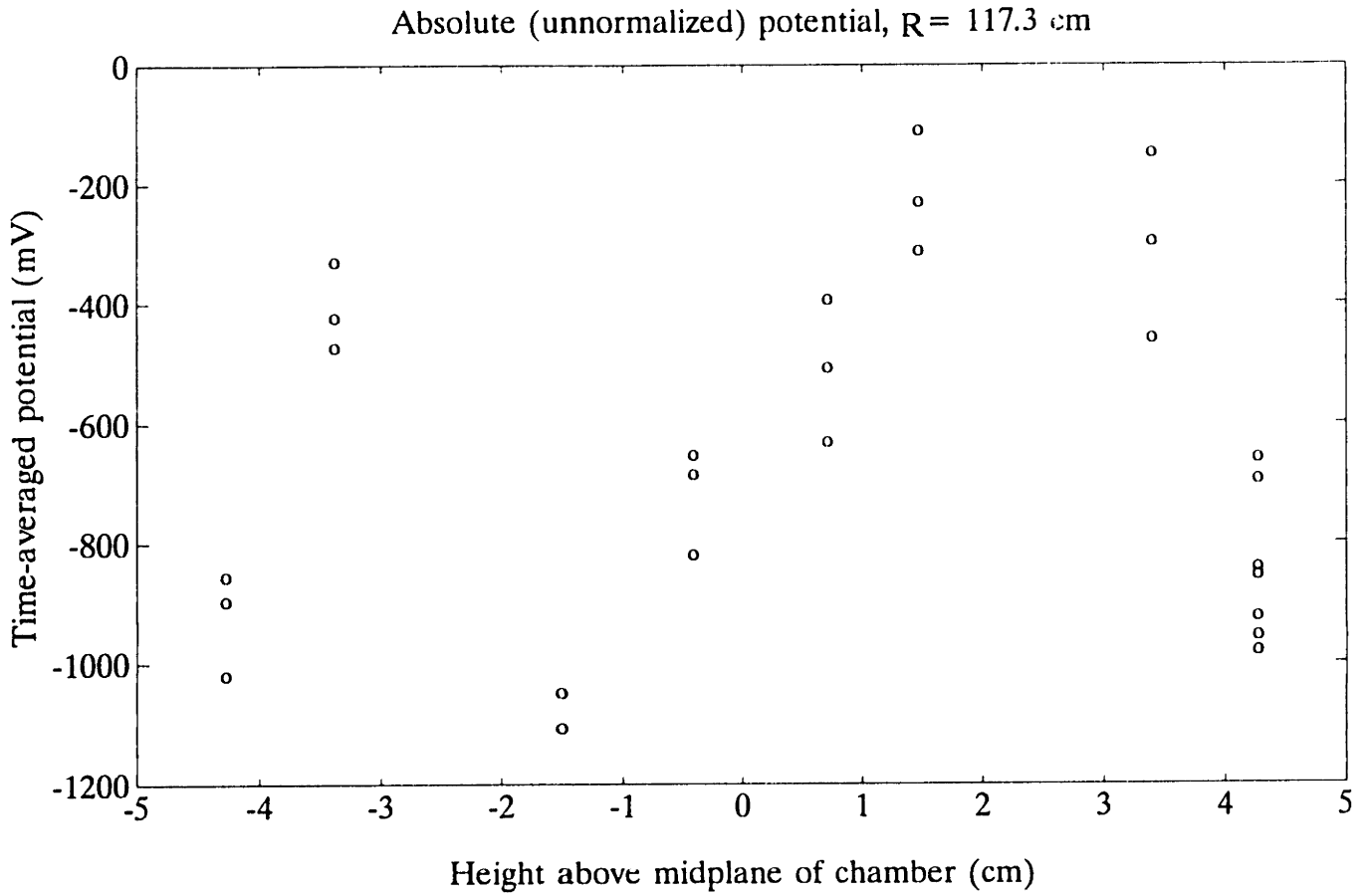
47

Figure 4-5: Time-averaged floating potential, major radius 117.3 cm.
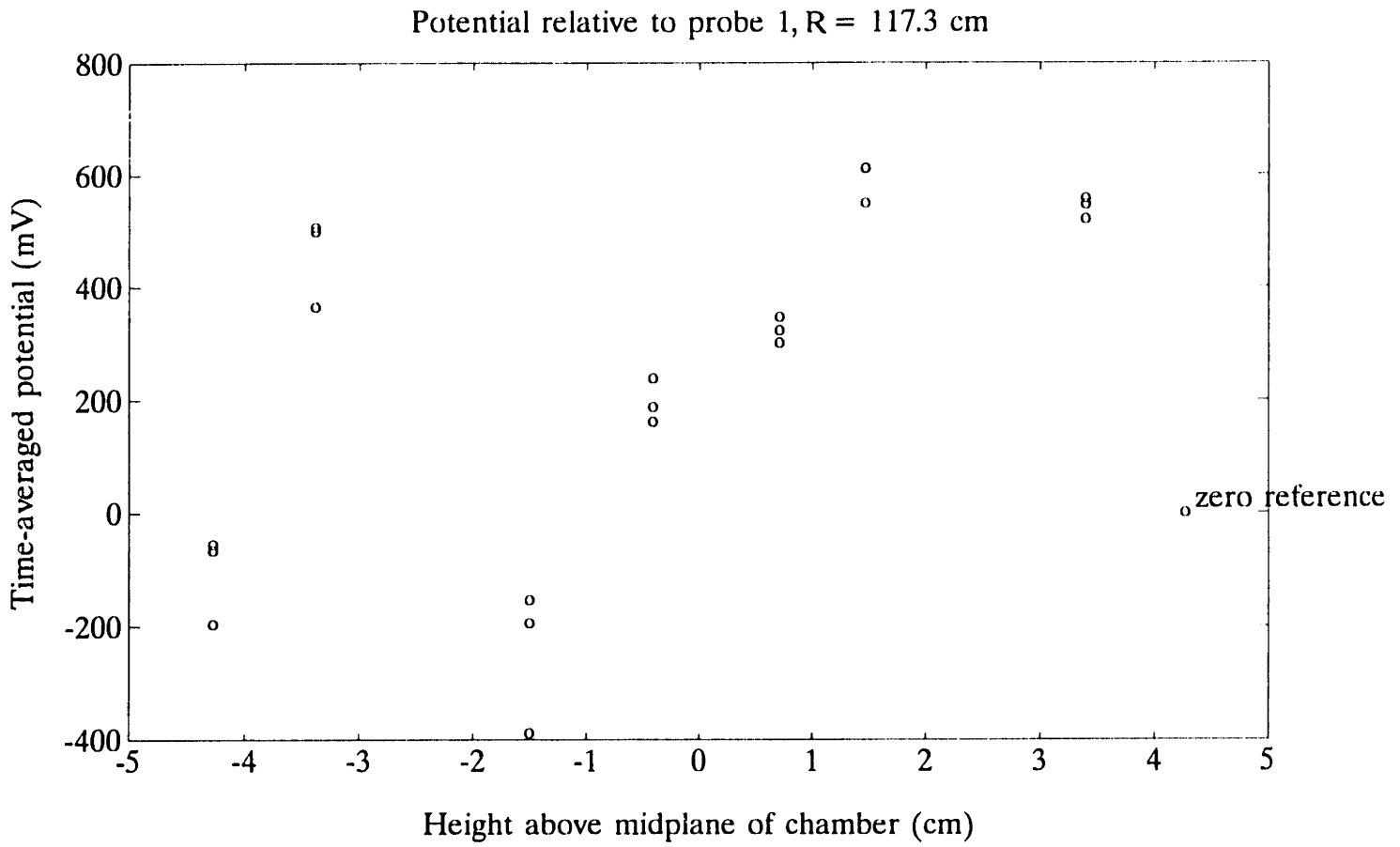
Figure 4-6: Time-averaged potential normalized to probe 1, major radius 117.3 cm.

Absolute (unnormalized) potential, R = 104.6 cm

Figure 4-7: Time-averaged floating potential, major radius 104.6 cm.

4.3.2 Experimental Data

Potential data have also been gathered at other major radii. These data did not appear

to be significantly improved by normalization, because the shot-to-shot variation in the

differences between the readings on two given probes were not significantly smaller than

the variations in the offset potential. Both absolute and normalized data are presented

here.

The results at $R = 117.3$ cm (Fig. 4-6) indicate an electric field with structure on the

Figure 4-8: Time-averaged potential normalized to probe 1, major radius 104.6 cm.

scale of the distance between probes. Therefore it is difficult to determine a particular value of E_v by looking at the plot. The potential fluctuates in space by as much as 1 V, and so the electric field clearly fluctuates as well. A fairly uniform trend (although it may only be a statistical illusion) seems to appear over a 4-cm length around the center of the probe array, where the slope of the potential, equal to the electric field, is 0.3 V/cm (1.0×10^{-3} statvolt/cm). In general, the slope does not appear to exceed 0.5 V/cm (1.7×10^{-3} statvolt/cm) at any point on the plot.

At $R = 117.3$ cm (Figures 4-7 and 4-8) the normalization appears to have little effect on the "random" spread of the data points. The potential varies on the same length scale as at $r = 117.3$ cm, but not as strongly. The differences appear to be on the order of 0.05 V/cm (1.7×10^{-4} statvolt/cm.

The data at $R = 94.4$ cm (Figures 4-9 and 4-10) show little evidence of any vertical electric field— the variation in the data points is large enough to where no trend is visible.

4.3.3 Plasma Drift

The presence of a vertical electric field E_v and a toroidal magnetic field $B_0 = 700$ gauss produce an E × B drift in the radial direction. The magnitude of the drift velocity,

$$v_{gc} = c\frac{E_v}{B_0} \tag{4.3}$$

is clearly nonuniform, as is its direction, due to the spatially varying vertical electric field which has been measured. This corresponds to a form of convective plasma drift, with velocities up to 7×10^4 cm/sec at $R = 117$ cm. At $R = 105$ cm, the strongest measured
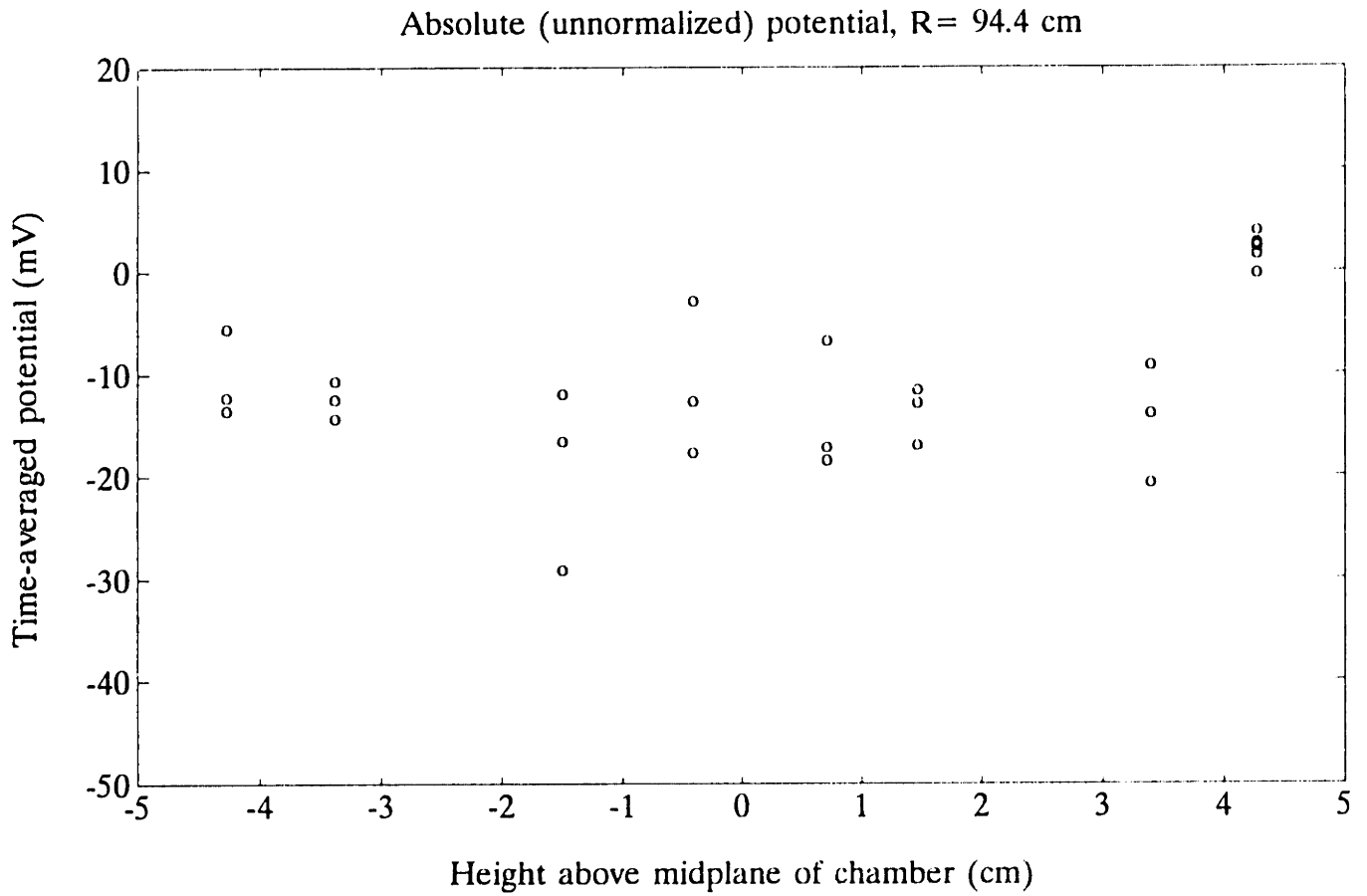
Figure 4-9: Time-averaged floating potential, major radius 94.4 cm.

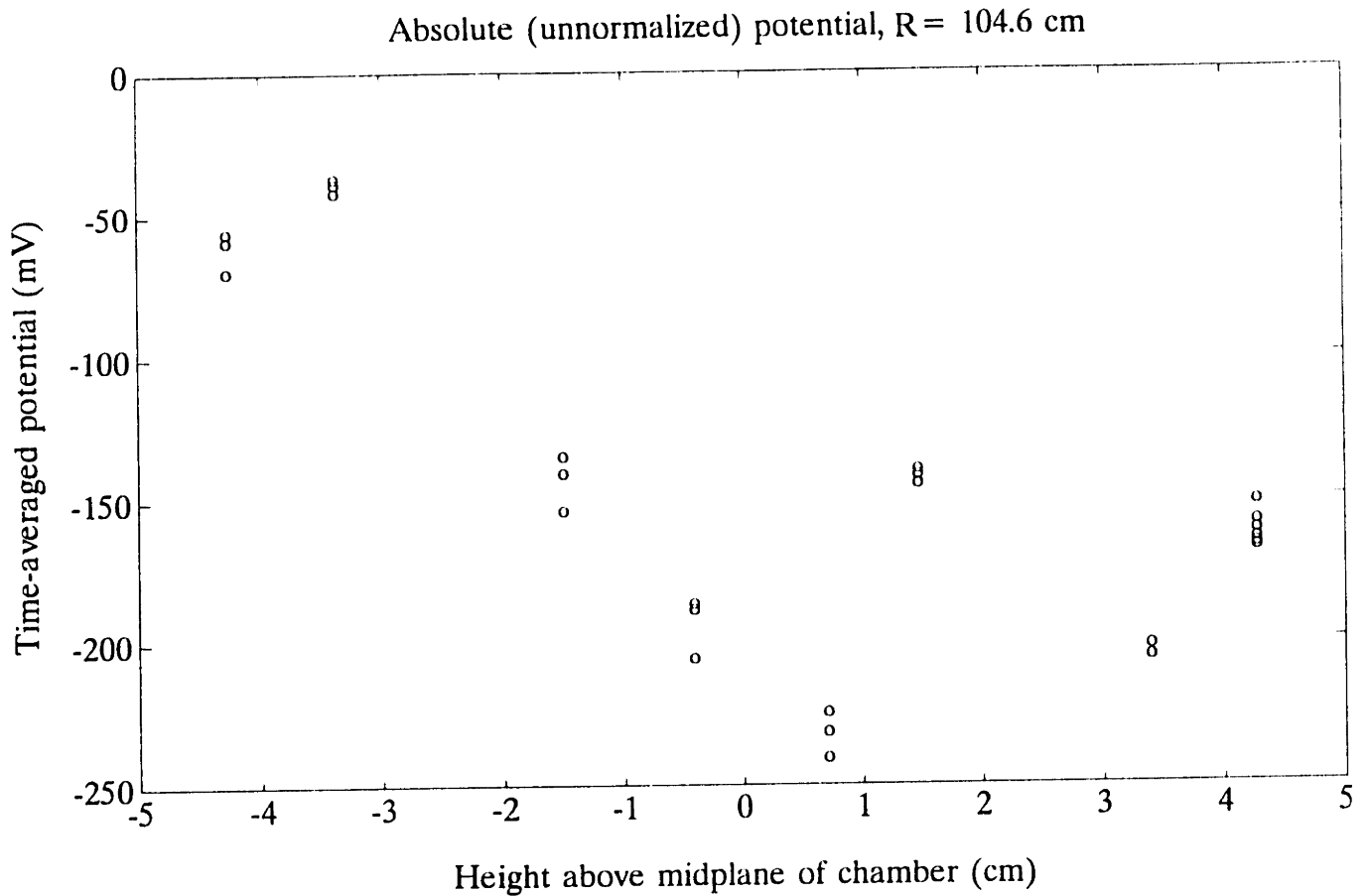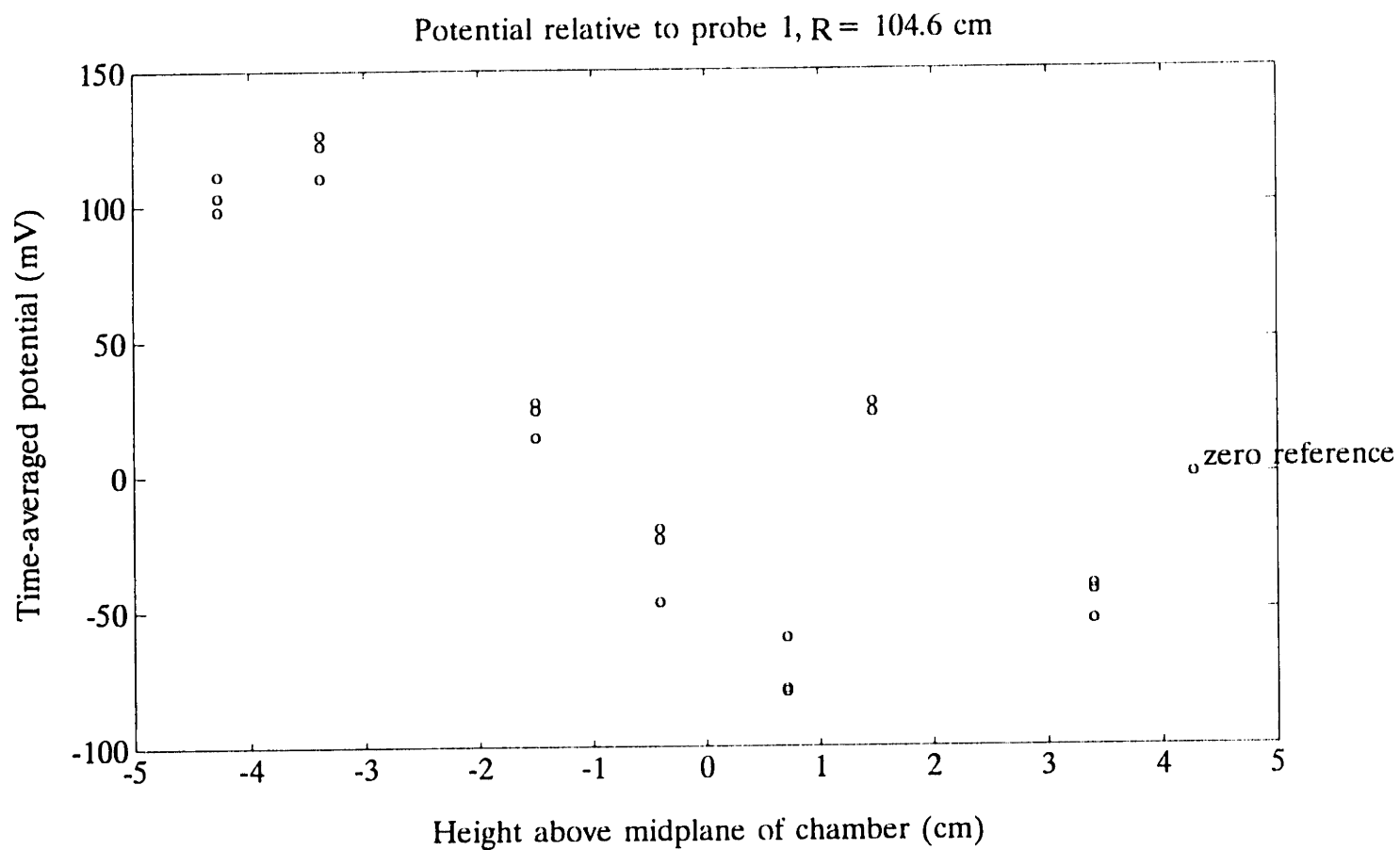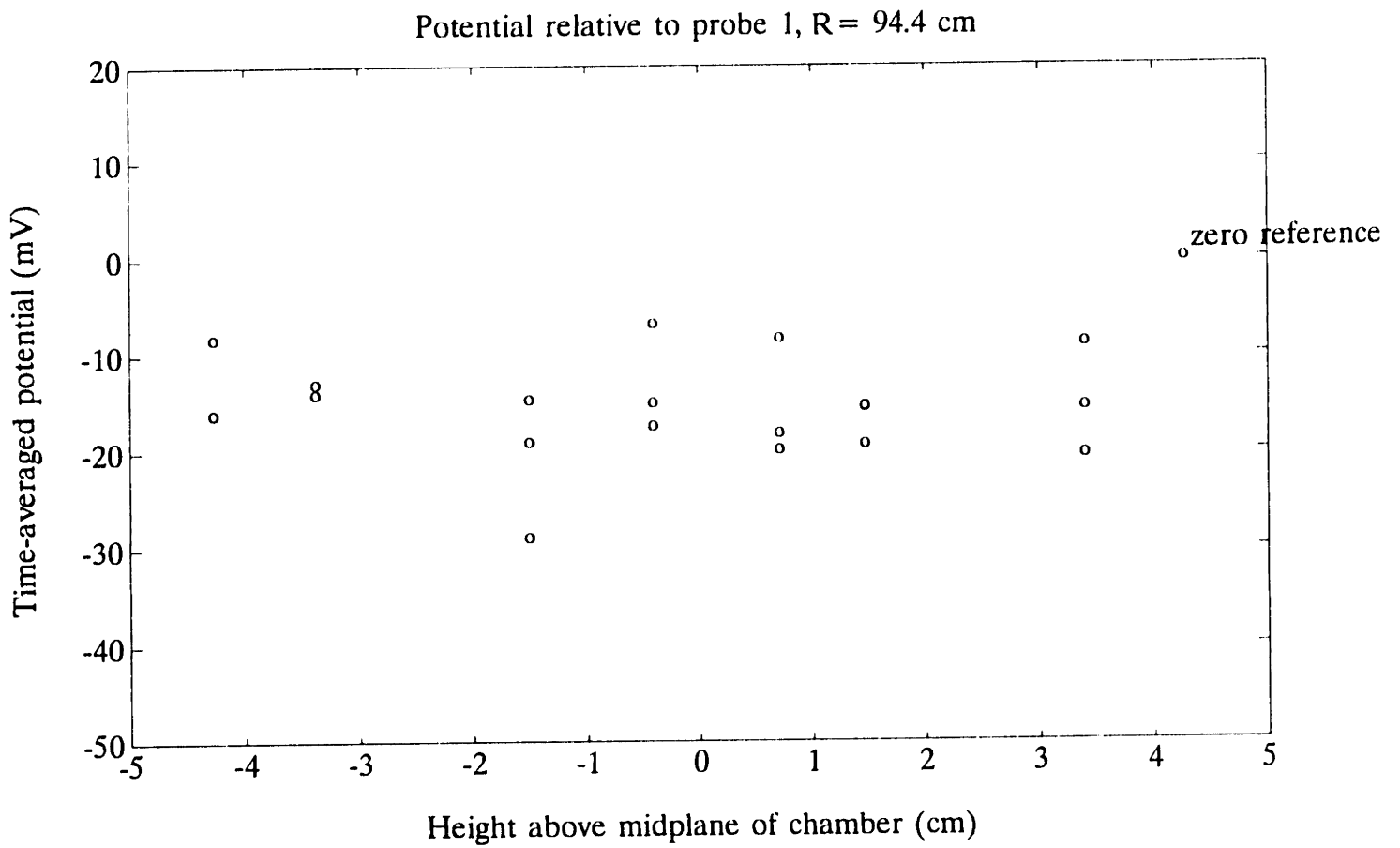Figure 4-10: Time-averaged potential normalized to probe 1, major radius 94.4 cm.

electric field corresponds to a drift velocity of 10^4 cm/sec.

The non-uniformity of $E_z(z)$, which actually changes sign in some cases, indicates that the plasma is undergoing a complex convective flow. The flow is radially outward at some locations and inward at others. The spatial scale of the changes of flow direction is on the order of 1–5 cm, as seen in Figures 4-6 and 4-8.

Chapter 5

Correlation Analysis

Plasma fluctuations are a phenomenon which occur with a finite spatial dimension as well as a time scale. Characteristic scale lengths for plasma turbulence include the density gradient scale length $\lambda_n \approx$ 3–5 cm, as well as the ion gyro radius $\rho_i \approx$ 0.3 cm. The probe spacing on the array of $\sim$0.9 cm allows fluctuations of lengths comparable to and greater than ρ_i to be measured.

A thorough analysis of turbulent fluctuations must examine simultaneous measurements at nearby points in space. This was done by analyzing correlations between signals from different probes during the same shot.

5.1 Mathematical Techniques

In order to examine the joint properties of two time signals, it is necessary to use a function which calculates quantitatively the resemblance between the two functions. The functions utilized here are statistical averages of multiplicative functions of Fourier transforms of the signal data. Data analysis was carried out using MATLAB software running

on a 486-based PC.

5.1.1 Cross-correlation Spectrum

The *cross-correlation spectrum* provides a measure of the degree to which individual frequency components of two time signals are correlated. To calculate the correlation spectrum between two time signals $a(t)$ and $b(t)$, the time signals are broken up into n finite intervals of equal duration. The Fourier transforms $\tilde{a}_i(\omega)$ and $\tilde{b}_i(\omega)$ are calculated for each of the intervals. The complex cross correlation $\mathcal{F}_{a,b}(\omega)$ between $a(t)$ and $b(t)$ is defined as follows:

$$\mathcal{F}_{a,b}(\omega) = \frac{\sum_{i=1}^{n} \tilde{a}_i(\omega)\tilde{b}_i^*(\omega)}{\sqrt{\sum_{i=1}^{n} \tilde{a}_i(\omega)\tilde{a}_i^*(\omega)}\sqrt{\sum_{i=1}^{n} \tilde{b}_i(\omega)\tilde{b}_i^*(\omega)}} \qquad (5.1)$$

Coherence function

The squared magnitude $\mathcal{F}\mathcal{F}^*$ of the cross-correlation spectrum is known as the *coherence function*, and varies between 0 and 1:

$$C_{a,b}(\omega) \equiv \mathcal{F}_{a,b}(\omega)\mathcal{F}_{a,b}^*(\omega) \qquad (5.2)$$

Two perfectly correlated signals have a coherence of unity, while totally uncorrelated signals have a coherence of zero. For two signals $a(t)$ and $b(t)$ to be "perfectly correlated" in the sense that $C_{a,b}(\omega) = 1$ for all ω, the signals need not be identical; in fact they may appear quite different. The coherence function may be unity even when some or all frequency components of the signals $a(t)$ and $b(t)$ are out of phase. Signals which are shifted in time with respect to each other thus remain perfectly correlated, as well as

signals which are sent through different frequency-dependent delay filters. In addition, the coherence function is independent of an arbitrary change in the amplitude of either signal. A detailed discussion of spectral analysis techniques can be found in Bendat and Piersol[1]

The utility of the coherence function is clear— it permits data which are gathered in different manners to be compared in a quantitative manner. Signals which the two series contain in common can be extracted from noise.

Phase of Cross-Correlation Spectrum

The phase ϕ of $\mathcal{F}_{a,b}(\omega)$ contains more subtle information than the coherence function. Its significance is that it is a measure of the phase difference between the ω-components of $a(t)$ and $b(t)$. However, it becomes statistically insignificant at points where the coherence is lower than approximately 0.5.

In practice, the utility of the phase of the cross-correlation is in the determination of a dispersion relation for wave activity. A linear relation between $\phi(\omega)$ and probe separation s at a given frequency ω would indicate a wave number $k(\omega)$ of

$$k(\omega) = \frac{d\phi(\omega)}{ds} \tag{5.3}$$

[1]J. Bendat, A. Piersol, *Random Data: Analysis and Measurement Procedures*, John Wiley & Sons, New York, 1986

5.1.2 Correlation Length

For fluctuations of a given frequency, the expected effect of a turbulent system is a damping of signals. Thus the coherence function $C_{a,b}(\omega)$ between two signals a and b, at a particular frequency ω, should decrease as a function of spatial separation of the probes producing the two signals. Assuming there are no nonlinear amplitude-dependent effects, the coherence should be reduced by a predictable fraction over a given distance. If that fraction is independent of $C_{a,b}(\omega)$ itself and independent of the particular position (i. e. the conditions giving rise to turbulence are spatially uniform), then the only possible profile is an exponential decay. Thus, if three time series a, b, and c are generated by probes at positions x_a, x_b, and x_c, where $x_a \leq x_b \leq x_c$, one would expect the following relation to hold:

$$C_{a,c}(\omega) = C_{a,b}(\omega) \exp[-\frac{x_c - x_b}{\lambda_C(\omega)}] \tag{5.4}$$

The constant $\lambda_C(\omega)$, a function of the medium and the particular frequency component being studied, is known as the *correlation length*. The number is generally determined experimentally from the coherence functions of several data sets. It should be noted that the concept of a correlation length does not have significant meaning unless the medium has the linearity and uniformity properties described above.

5.2 Analysis of Experimental Data

This section contains the results of correlation analysis of experimental data. The complex cross-correlation function between two simultaneous signals from different probes

was calculated, for all probe combinations, using 256-point Fourier transforms (In the notation of the previous section, $n = 128$). Both the coherence functions and the phases of the cross-correlation functions were studied as a function of probe separation. The coherence functions were also examined as a function of frequency.

5.2.1 Contour Plots of Coherence Functions

The behavior of the coherence function as both probe separation and frequency [2] are varied is shown here as a series of contour plots, where the contours represent paths of constant coherence. The first set (Figures 5-1 through 5-4) were produced by examining the coherence functions of one signal (based on 256-point FFTs) from each of probes 2-10 with a simultaneous signal from probe 1; there are thus seven data arrays contained in each plot. Intermediate values were determined by interpolation, and generated by the MATLAB program. Each contour plot contains data taken at a fixed radial position.

The second set of plots, Figures 5-5 through 5-8, are composite plots, which include many more data sets than the first. They are produced by averaging the coherence functions between data from many sets of two probes (over six shots of data). For example, the array corresponding to a probe separation of two probes (1.9 cm) is an average of the data from probes 2 and 4, 4 and 6, 5 and 7, and 7 and 9. The purpose of averaging over many shots is to "clean up" the representation by smoothing out the random error. In doing so, however, we are assuming that the plasma is uniform over the

---

[2] Appendix B shows x-y plots of coherence as a function of frequency alone at different radii and probe separations.
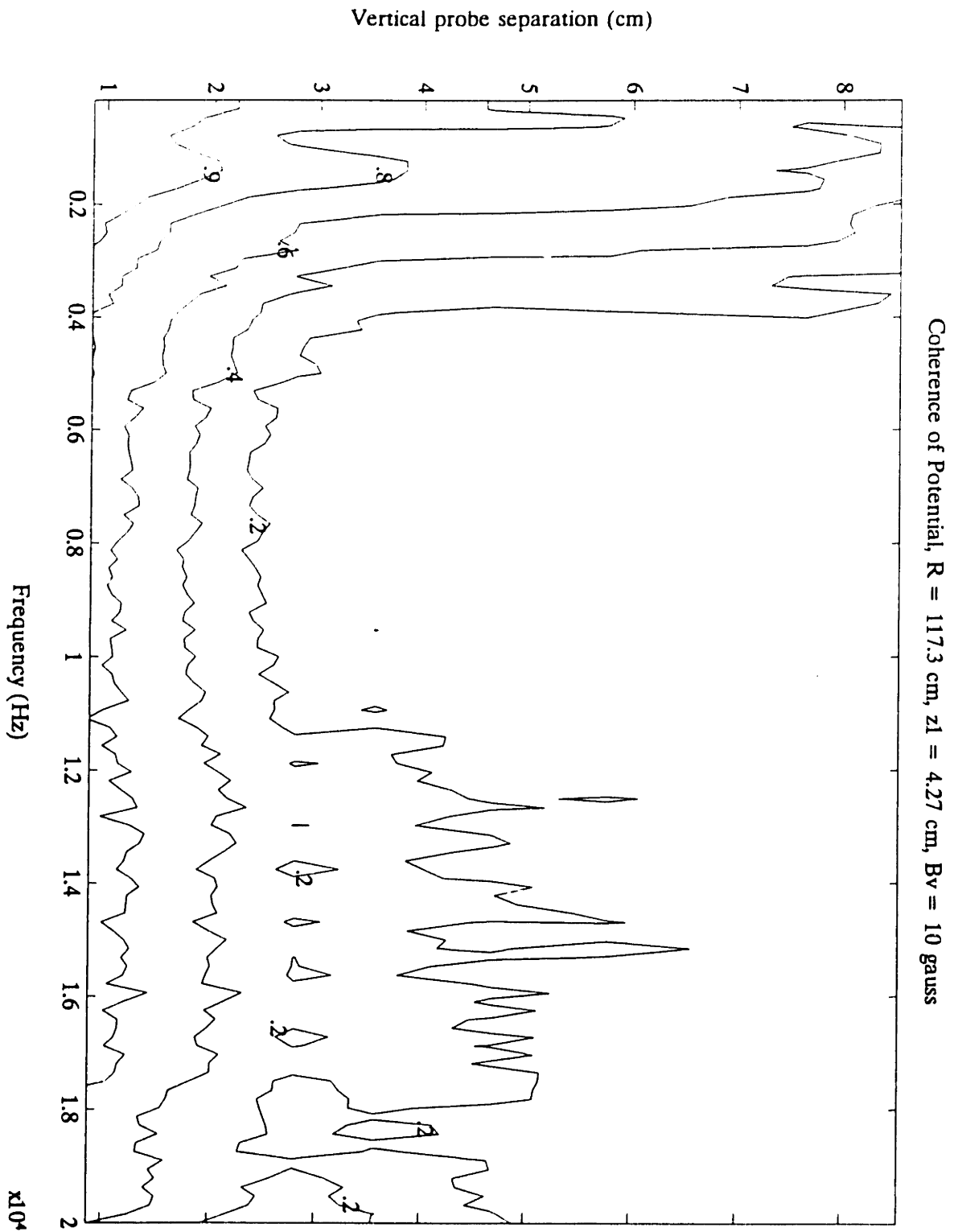
Figure 5-1: Contour plot of coherence of potential. Major radius = 117.3 cm, Vertical field B_v = 10 gauss. Data obtained from seven sets of two arrays each. Each set contains data from probe 1 and from another probe.
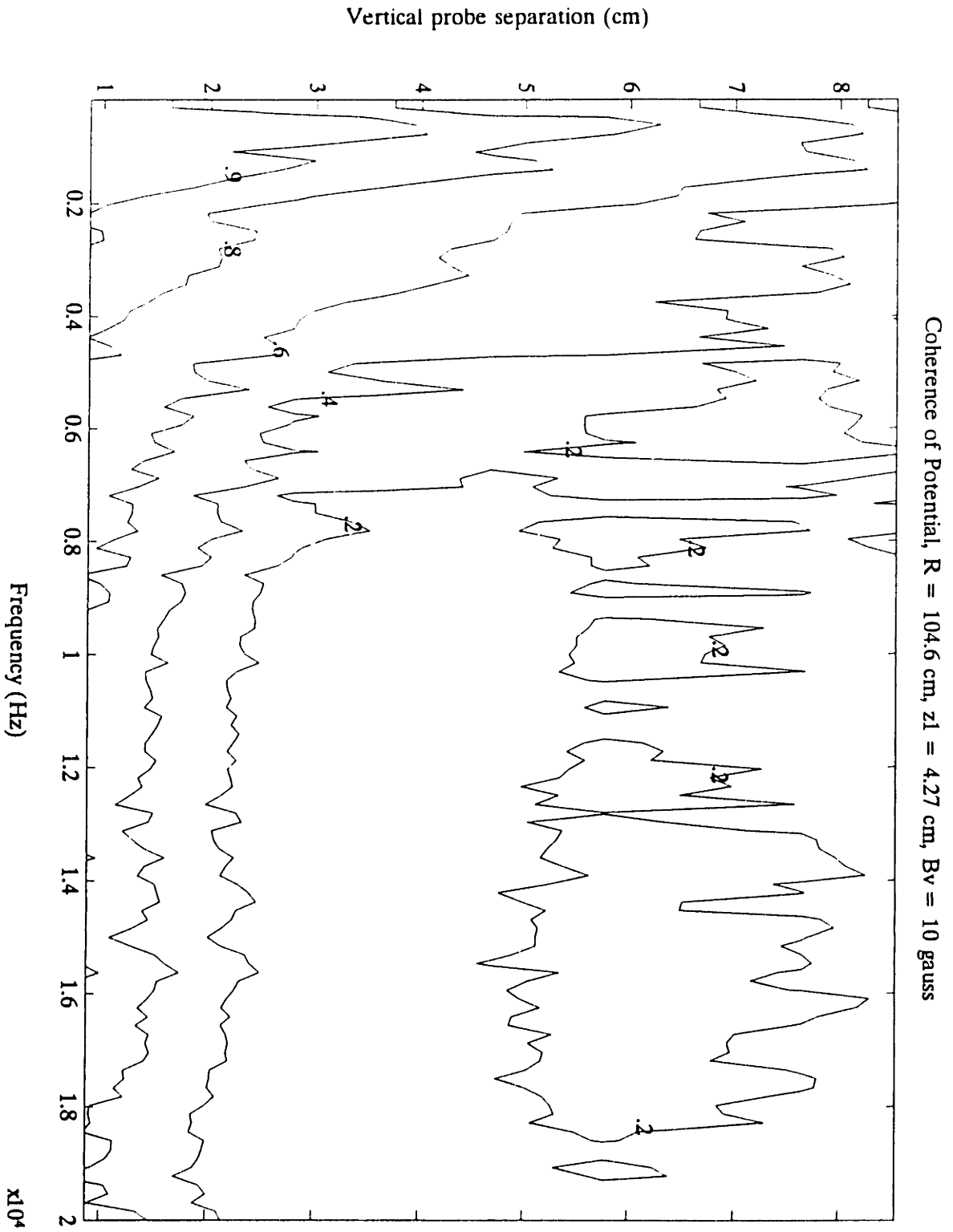
61

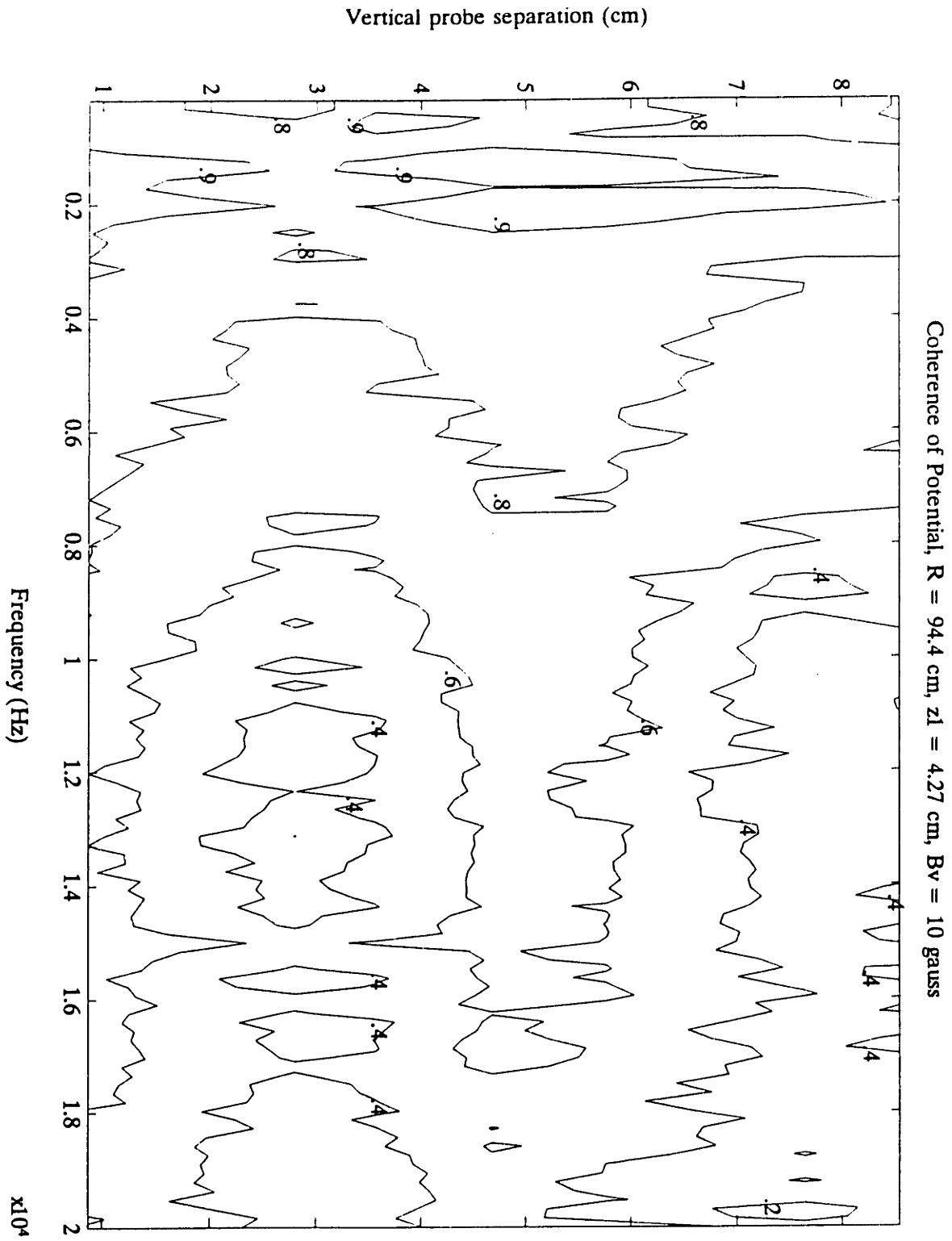Figure 5-2: Contour plot of coherence of potential. Major radius = 104.6 cm.

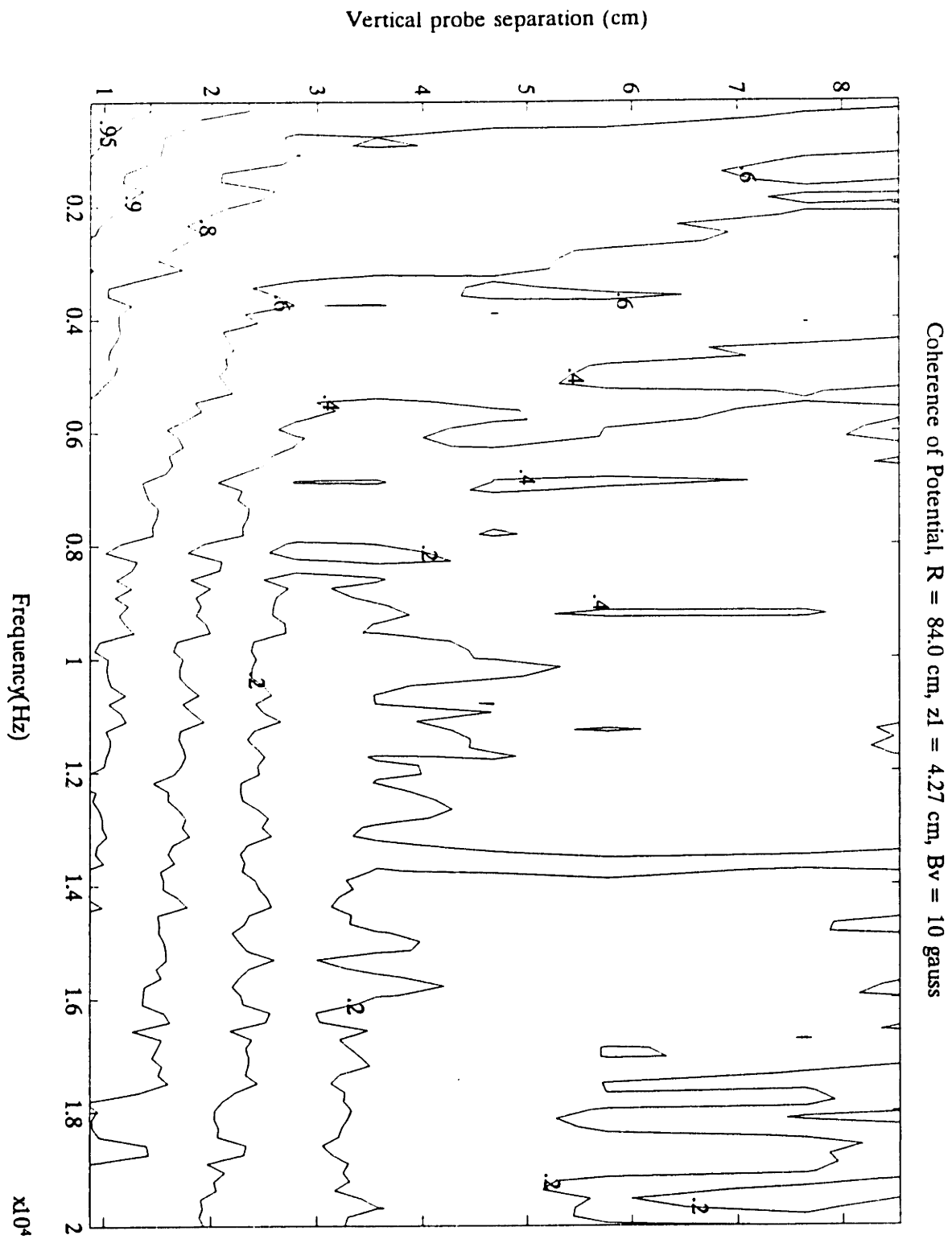Figure 5-3: Contour plot of coherence of potential. Major radius = 94.4 cm.

Figure 5-4: Contour plot of coherence of potential. Major radius = 84.0 cm.

length of the probe array. Specifically, the assumption is that the difference between the coherence between data at probes 2 and 4 and between probes 7 and 9 can be attributed to random error alone.

5.2.2 Phase of Cross-Correlation Functions

Because the experimental data show so little coherence in most frequency regions, the phase of the cross-correlation function is not a very significant datum. However, the signals are highly correlated at low frequencies, so it is useful to examine the phase of $\mathcal{F}(\omega)$ in this region. Selecting a frequency of 1875 Hz (within the coherent region at all radii and probe separations), plots of $\phi(\omega = 2\pi \cdot 1875 \text{ sec}^{-1})$ versus probe separation s are shown as Figures 5-9 through 5-12 for the four radial positions studied. The plots are obtained from the 1875 Hz data point of cross-correlation functions based on 128-point FFTs of the original experimental data.

As can be seen in the figures, the plots all show a slight increase in ϕ as s increases, but this trend is barely discernable because of large random errors in the individual data points. The trend appears to be on the order of $d\phi/ds \approx (0.01 \pm 0.005) \text{ cm}^{-1}$.

Because signals taken at major radius $R = 94.4$ cm appeared highly coherent at longer distances and higher frequencies than anywhere else, phase data should be significant at higher frequencies. A plot of ϕ versus s at frequency 8125 Hz and radius 94.4 cm is shown as Fig. 5-13. The phase shift shows no identifiable trend at this frequency; the slope appears to be zero.
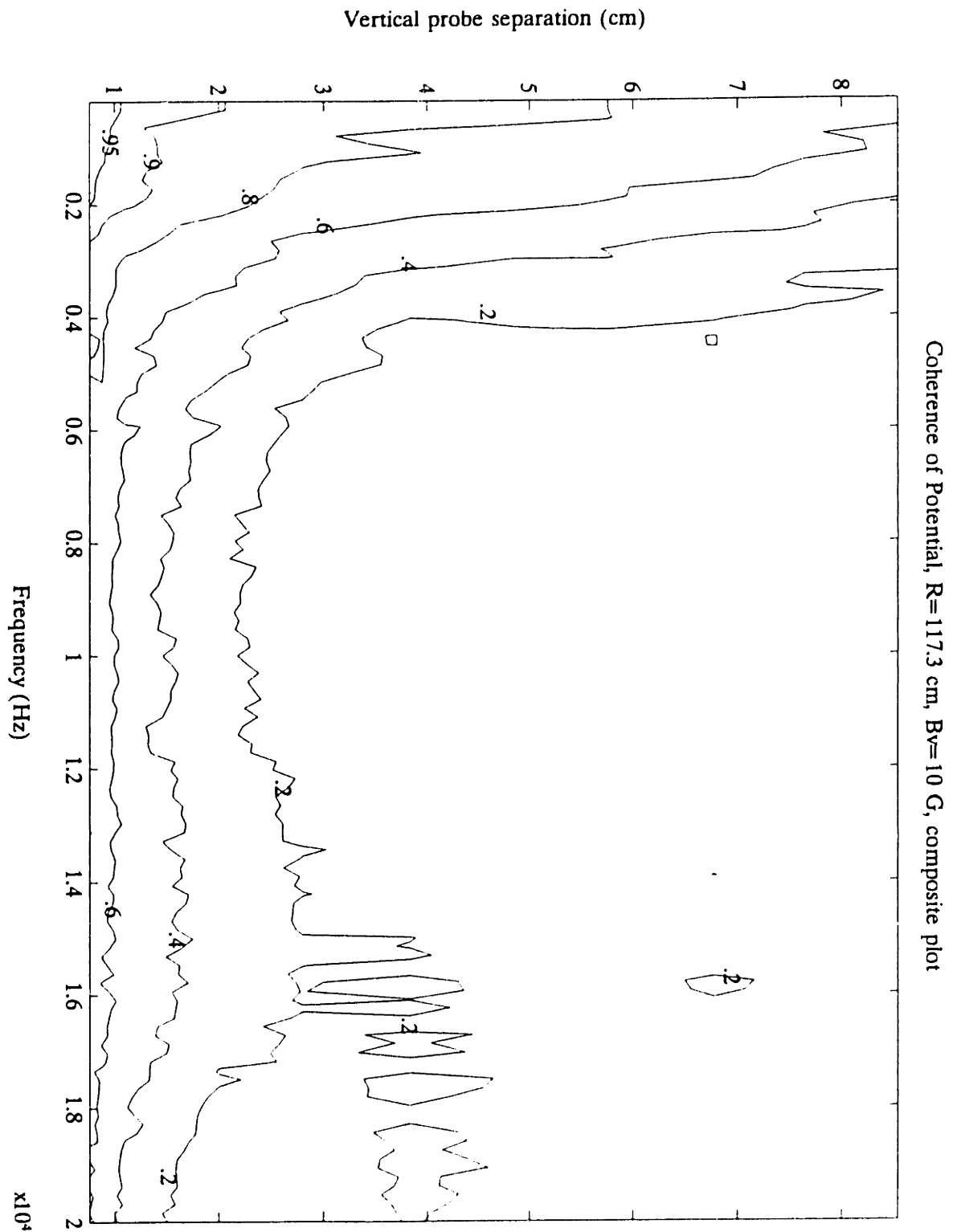
Figure 5-5: Contour plot of coherence of potential. Major radius = 117.3 cm, $B_v = 10$ gauss. Composite plot using data from 26 sets of two arrays each.
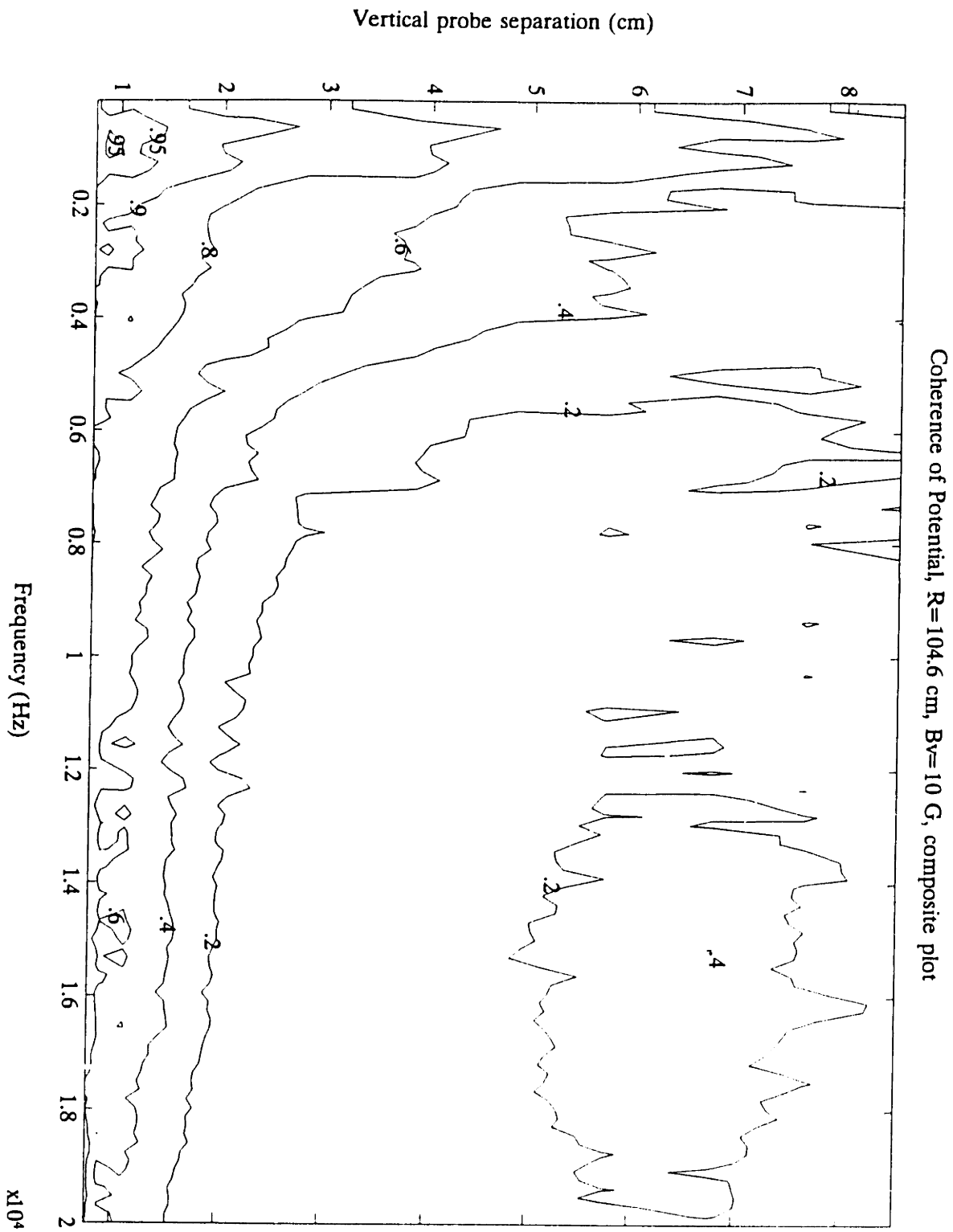
Figure 5-6: Composite contour plot of coherence of potential. Major radius = 104.6 cm.
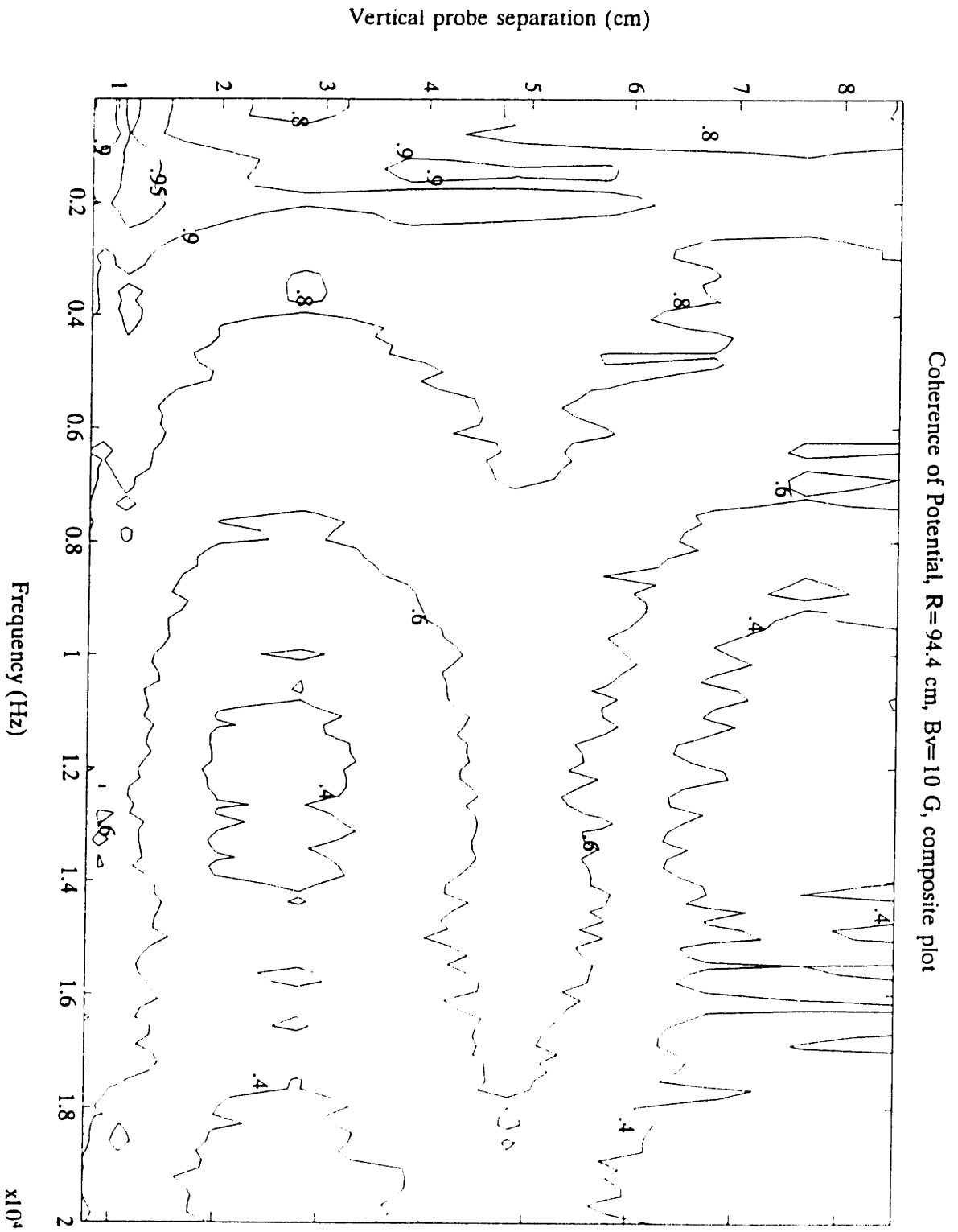
Figure 5-7: Composite contour plot of coherence of potential. Major radius = 94.4 cm.
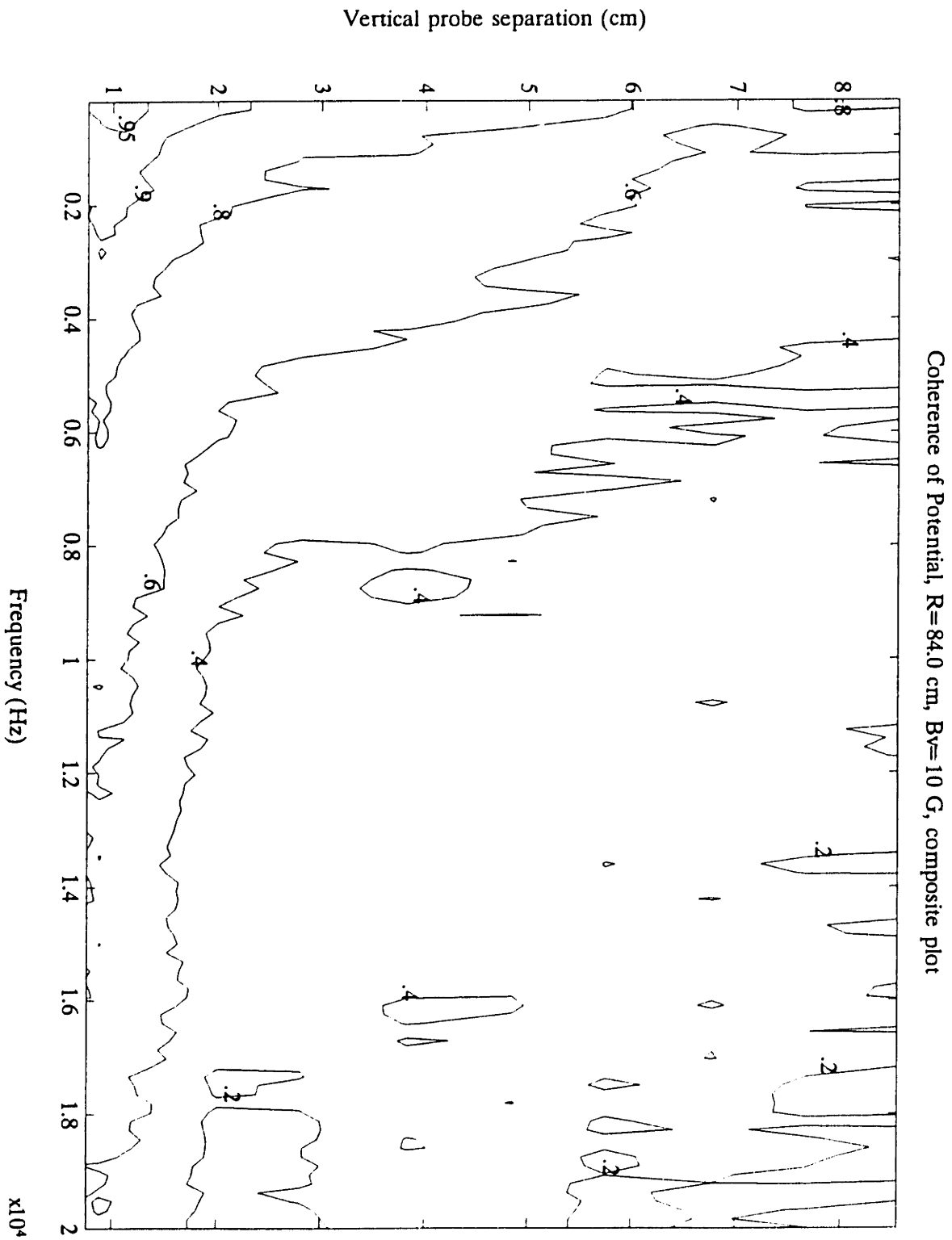
Figure 5-8: Composite contour plot of coherence of potential. Major radius = 84.0 cm.
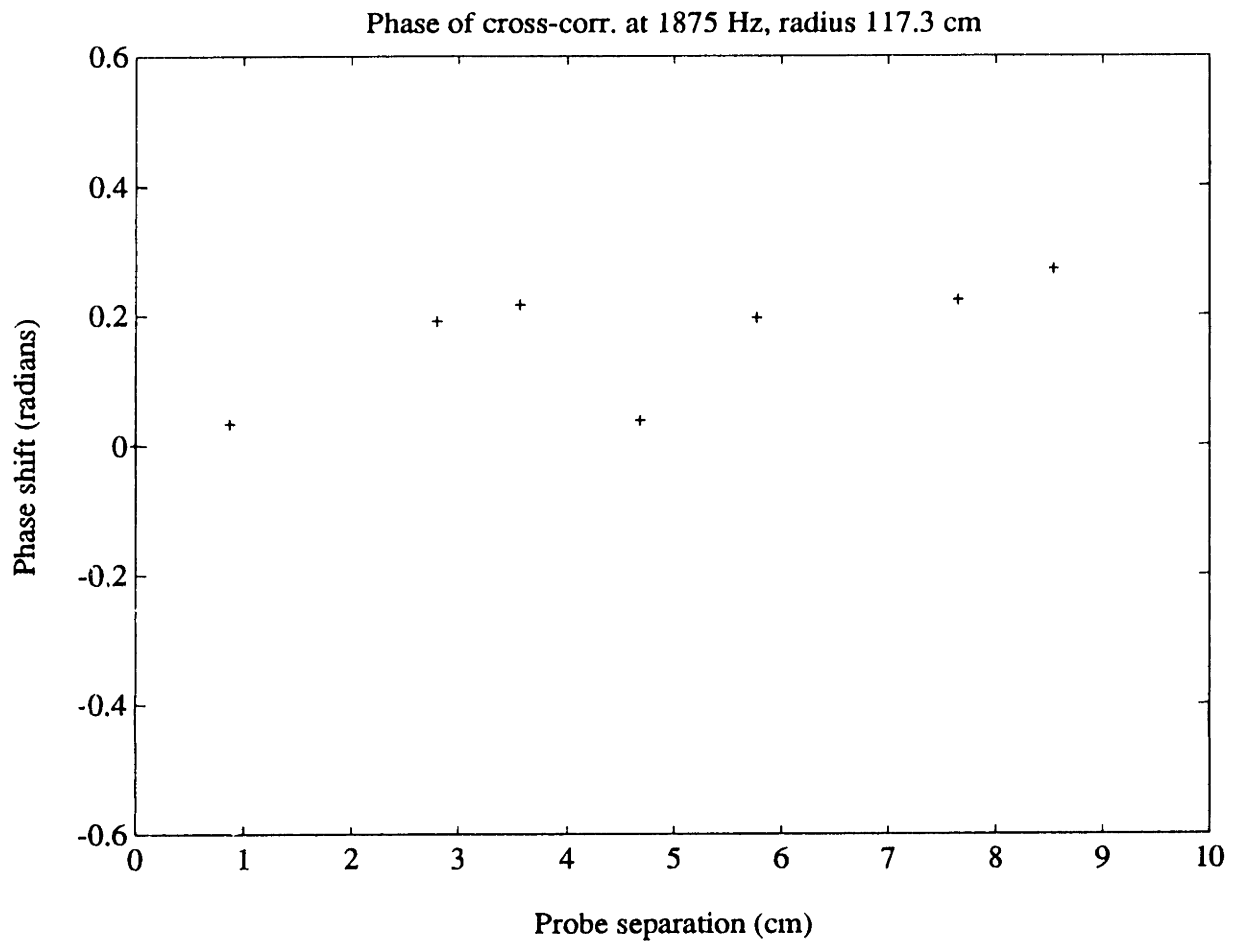
Figure 5-9: Phase of cross-correlation spectrum at 1875 Hz versus probe separation. Major radius 117.3 cm.

Figure 5-10: Phase of cross-correlation spectrum at 1875 Hz versus probe separation. Major radius 104.6 cm.
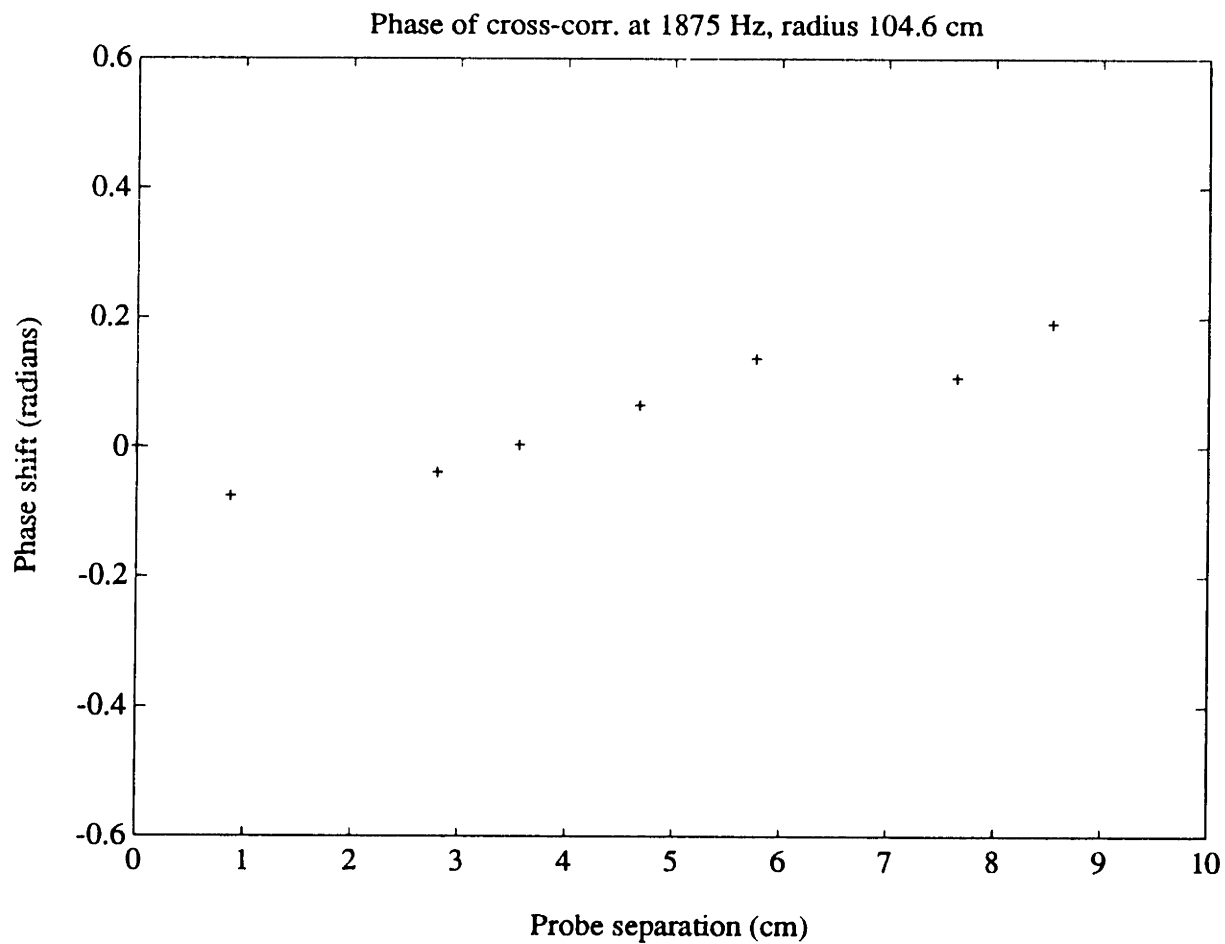
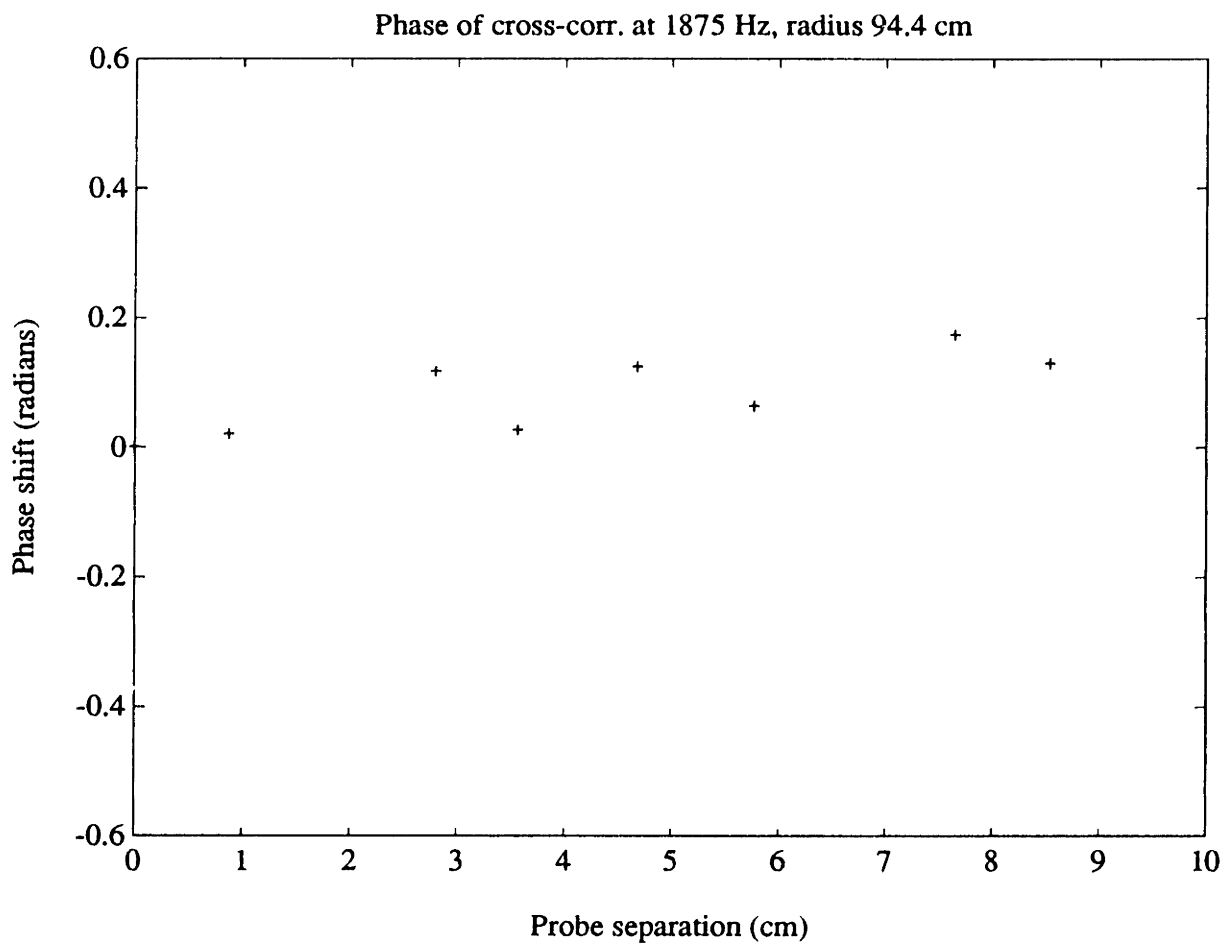Phase of cross-corr. at 1875 Hz, radius 94.4 cm

Figure 5-11: Phase of cross-correlation spectrum at 1875 Hz versus probe separation. Major radius 94.4 cm.
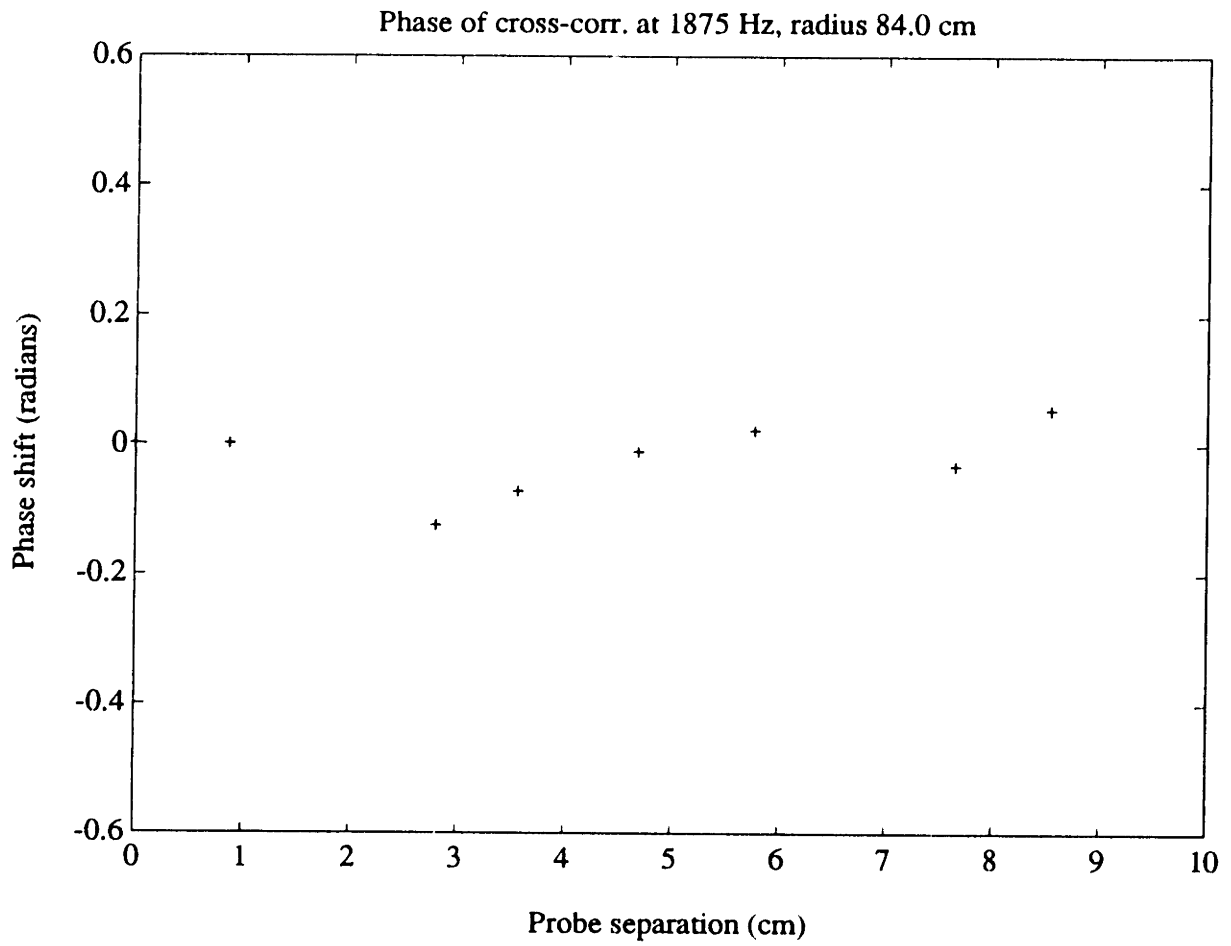
Figure 5-12: Phase of cross-correlation spectrum at 1875 Hz versus probe separation. Major radius 84.0 cm.
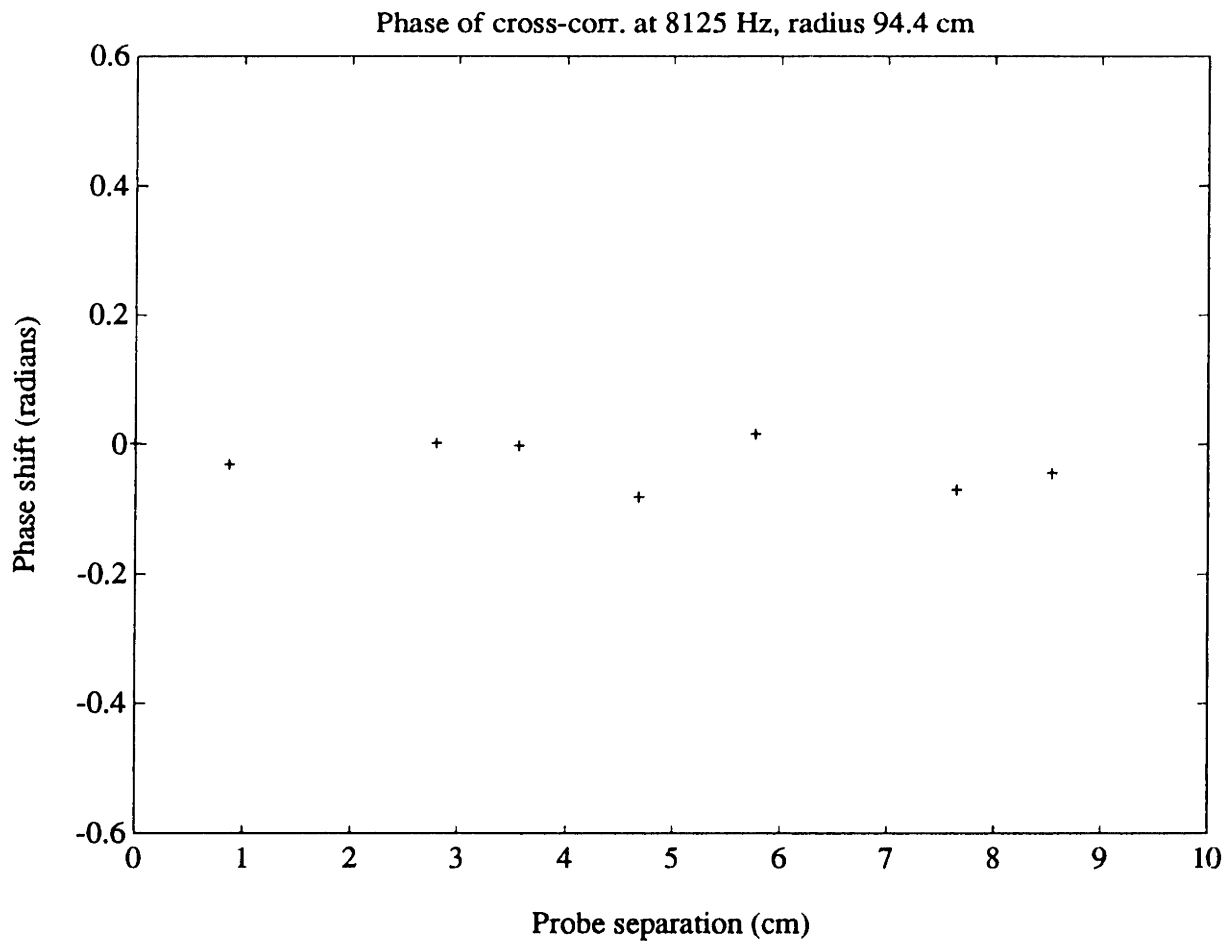
Figure 5-13: Phase of cross-correlation spectrum at 8125 Hz versus probe separation. Major radius 94.4 cm.

5.3 Interpretation of Results

In general, the results of the correlataion analysis indicate that plasma fluctuations along the vertical dimension of the HELIMAK plasma are turbulent rather than wave-like. Moreover, the turbulence exhibits a complex spatial structure in some regions of the plasma (Fig. 5-7). These results are discussed below.

5.3.1 Correlation Lengths of Potential Fluctuations

Correlation lengths vary greatly by frequency, and in different ways at different radial positions. At a major radius of 94.4 cm (data shown as Fig. 5-7), on the inner slope of the density peak, the correlation length is undefined because the coherence does not decay exponentially with distance— indeed, at probe separations between 3 and 6 cm, it actually *increases* with probe distance, indicating a serious nonlinearity in the plasma at that radius. This is not a position-dependent effect. It is equally apparent in the composite plot (Fig. 5-7) as in the plot of coherence with probe 1 signals only (Fig. 5-3). The observation of this multiple length-scale spatial coherence is one of the most intriguing results of this thesis.

At other radii, the correlation length was better defined. At 117 cm, in the outer low-density region, (Fig. 5-5), λ_C was greater than 10 cm for fluctuations in the 1 kHz range, dropping to about 8–10 cm in the 3 kHz range. $\lambda_C \approx 5$ cm around 4 kHz, dropping rapidly in this range to approximately 1 cm around 6 kHz, where it appears to level off and remain up to 20 kHz, the high-frequency limit of the data. Due to the unevenness

of the data, these numbers have a substantial error attached to them— $\pm 25\%$.

On the outer slope of the density peak, at $R = 105$ cm (Fig. 5-6), the coherence plot is not dramatically different from the one in the low-density region. Once again, λ_C is greater than 10 cm at the low-frequency end of the spectrum. However, the correlation length does appear to drop off at somewhat lower frequencies than in the low-density region. Between 2 and 4 kHz, λ_C is approximately 6 cm. Between 4 and 6 kHz, the correlation length drops rapidly to 2 cm. At 8 kHz, $\lambda_C \approx 1$ cm, and it drops slowly through the rest of the spectrum to about 0.7 cm. Between 10 and 20 kHz, a small complex structure (less vividly apparent than at $R = 94$ cm) shows as a region of increased coherence at probe separations $5 \leq s \leq 8$ cm.

As mentioned above, the coherence on the inner slope of the density peak ($R = 94$ cm) exhibits a complex structure. At no frequency does it decrease steadily with increasing probe separation. It is thus impossible to describe the data with a simple correlation length at any frequency. Signals become highly coherent at a probe separation of 5 cm, regardless of the absolute position of the probes. It is unclear what physical process is leading to this. One possible explanation is that the fluctuations have a very long extent along the helical field lines, and wrap completely around the torus, returning to the same toroidal angle ϕ displaced by Δz:

$$\Delta z = 2\pi R \frac{B_z}{B_\phi} \tag{5.5}$$

$$= \frac{593\text{cm} \cdot 10\text{gauss}}{700\text{gauss}} \tag{5.6}$$

$$\approx 8\text{cm} \tag{5.7}$$

which is relatively close to 5 cm, where the high-coherence readings occur.

The inner low-density region (Fig. 5-8) shows behavior somewhat similar to the outer one. Ar $R = 84$ cm, the correlation length is again greater than 10 cm at 1 kHz, and drops to about 10 cm at 2 kHz. However, it remains high (5–10 cm) at frequencies as high as 8 kHz. Higher than 10 kHz, λ_C drops to approximately 2 cm.

5.3.2 Evidence that Potential Fluctuations do not Represent Vertical Wave Activity

In this section, evidence is presented which indicates that the potential fluctuations studied here are not caused by plasma waves.

The phase data at different radii indicate that if there is wave activity at length scales no smaller than the distance between probes, it occurs with a wave number $k = (0.01 \pm 0.005)$ cm^{-1}. This corresponds to a wavelength of approximately 600 cm. Not only is this length nearly two orders of magnitude greater than the correlation lengths at the frequency studied, but it is several times longer than the height of the VTF vacuum chamber.

The higher-frequency component studied in the highly nonlinear case (Fig. 5-13) shows no sign whatsoever of a nonzero wave number. Clearly, the potential fluctuations studied here do not indicate the presence of vertically propagating waves.

77

Chapter 6

Conclusions

The most general result of these experiments has been that the plasma exhibits strikingly different qualities at different radial positions in the chamber, and that the inner and outer slopes of the density peak are dissimilar.

The largest levels of fluctuation activity were found in the outermost, low-density region. The amplitude of fluctuations steadily increased with major radius, with the smallest levels, lower by a factor of six, found in the inner low-density region. The density peak appears to be a dividing line between regions of high and low fluctuation activity.

The steady-state electric field also exhibits a change of behavior near the density peak. In the outer regions, the electric field shows violent oscillations in space, whereas it is near zero at inner radii. The large spatial variations in the electric field indicate the presence of radial convection flows in the plasma. Future experiments with a larger array of amplifier channels are necessary to explain a significant shot-to-shot variation discovered in the local floating potential.

The only measurement taken which appeared to be fairly independent of radial position was the shape of the fluctuation auto-power spectrum, which was similar at all radii, except for a low, broad peak which occurred only on the slopes of the density peak. At frequencies above 2 kHz, the plots show a practically identical decay according to a $1/\omega^2$ power law.

Coherence functions between signals taken at different vertical locations were analyzed in an effort to understand the spatial structure of the fluctuations at different frequencies. The results of this analysis were somewhat surprising. The structure of the coherence function appeared very similar in both the inner and outer low-density regions, even though the fluctuation amplitudes at the two locations were very different. The correlation lengths are on the order of 5-10 cm at frequencies below 5 kHz, and drop to around 1 cm at higher frequencies.

An interesting effect was observed at radii on the slopes of the density peak, more prominently on the inner slope. The coherence increases briefly but significantly with probe separation in the 5 cm range. This correlation spectrum cannot be characterized by a simple coherence length, but it may be explained if the turbulent fluctuations wrap around the torus along the helical field lines, returning to the same toroidal angle at 5 cm above the initial height. Future experiments which might test this hypothesis are possible. One could investigate it by varying B_v to determine whether the separation between high-coherence regions changes in a comparable way.

At a selected frequency, the phase of the cross-correlation function was calculated

for different radii and probe separations to determine whether or not the fluctuations represented wave activity. Because the wave numbers calculated from the measurements corresponded to wavelengths nearly two orders of magnitude longer than the coherence length (and much larger than the vacuum chamber), it was concluded that there was no evidence that the fluctuations represented dispersive wave activity.

Appendix A

Semi-Logarithmic Plots of Frequency Spectra

This section contains semi-logarithmic plots of the data presented in Section 4.2.
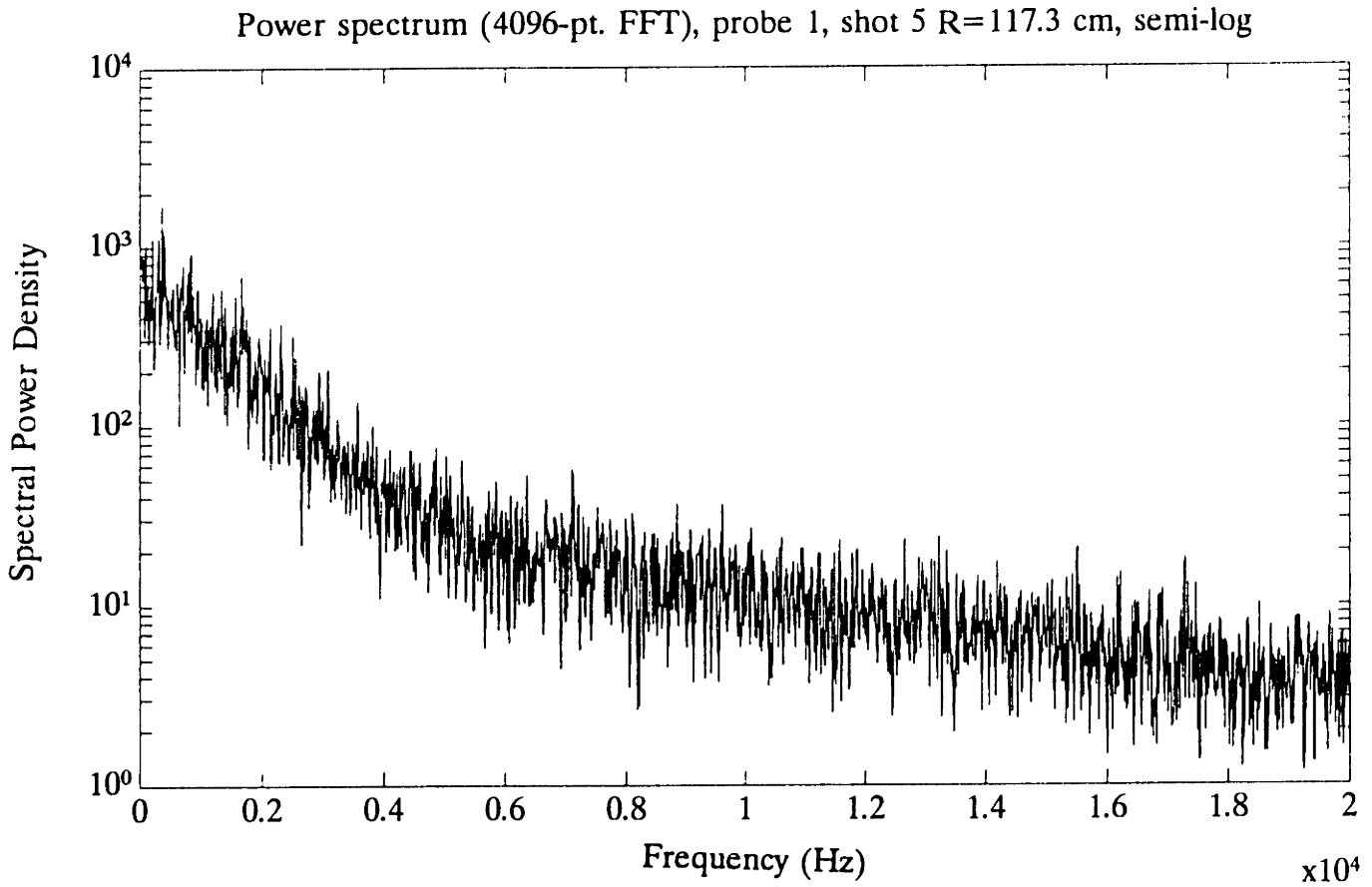
Figure A-1: Semi-logarithmic plot of fluctuation power spectrum. Major radius 117.3 cm. Composite of four 8192-point FFTs.
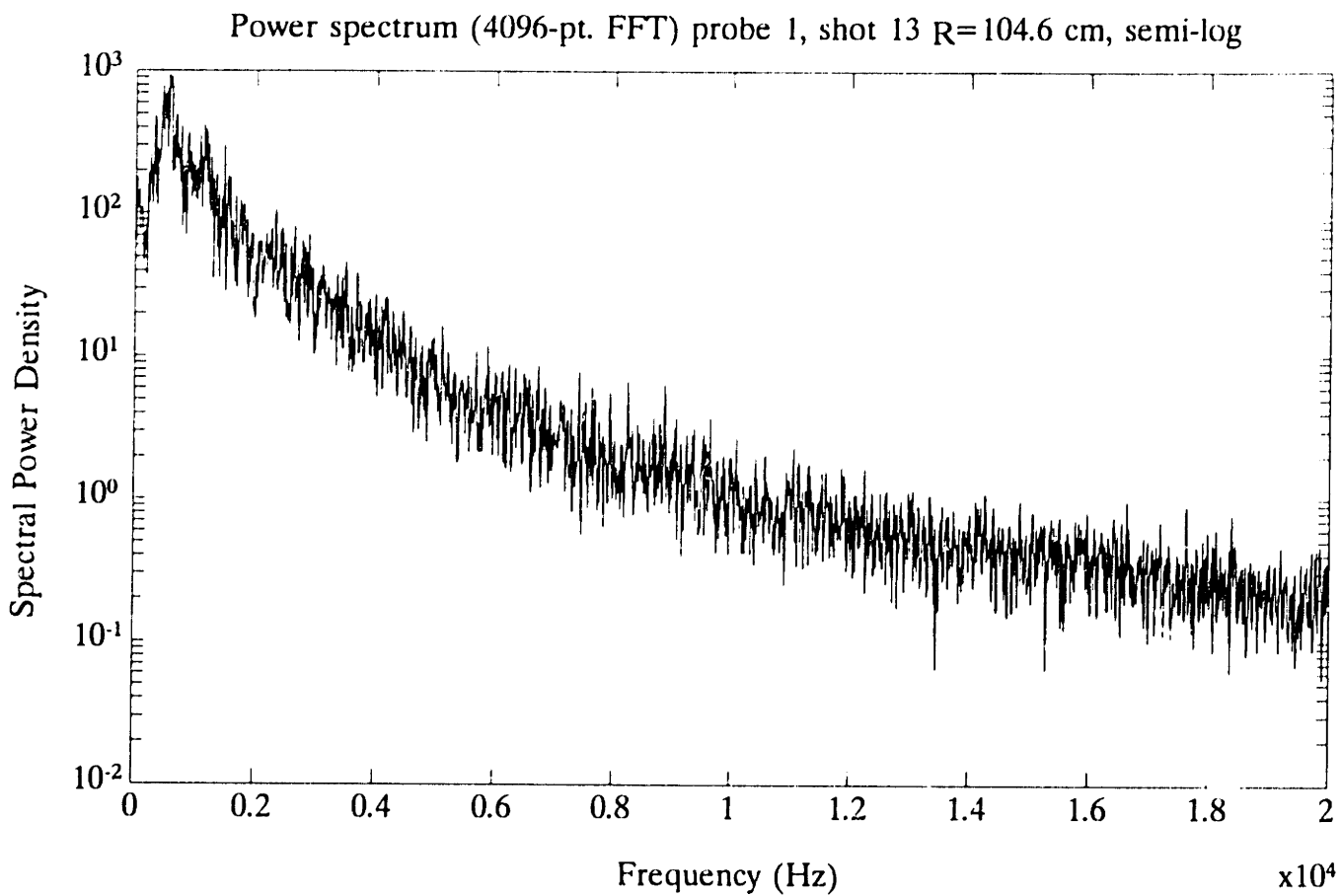
Figure A-2: Semi-logarithmic plot of fluctuation power spectrum. Major radius 104.6 cm.
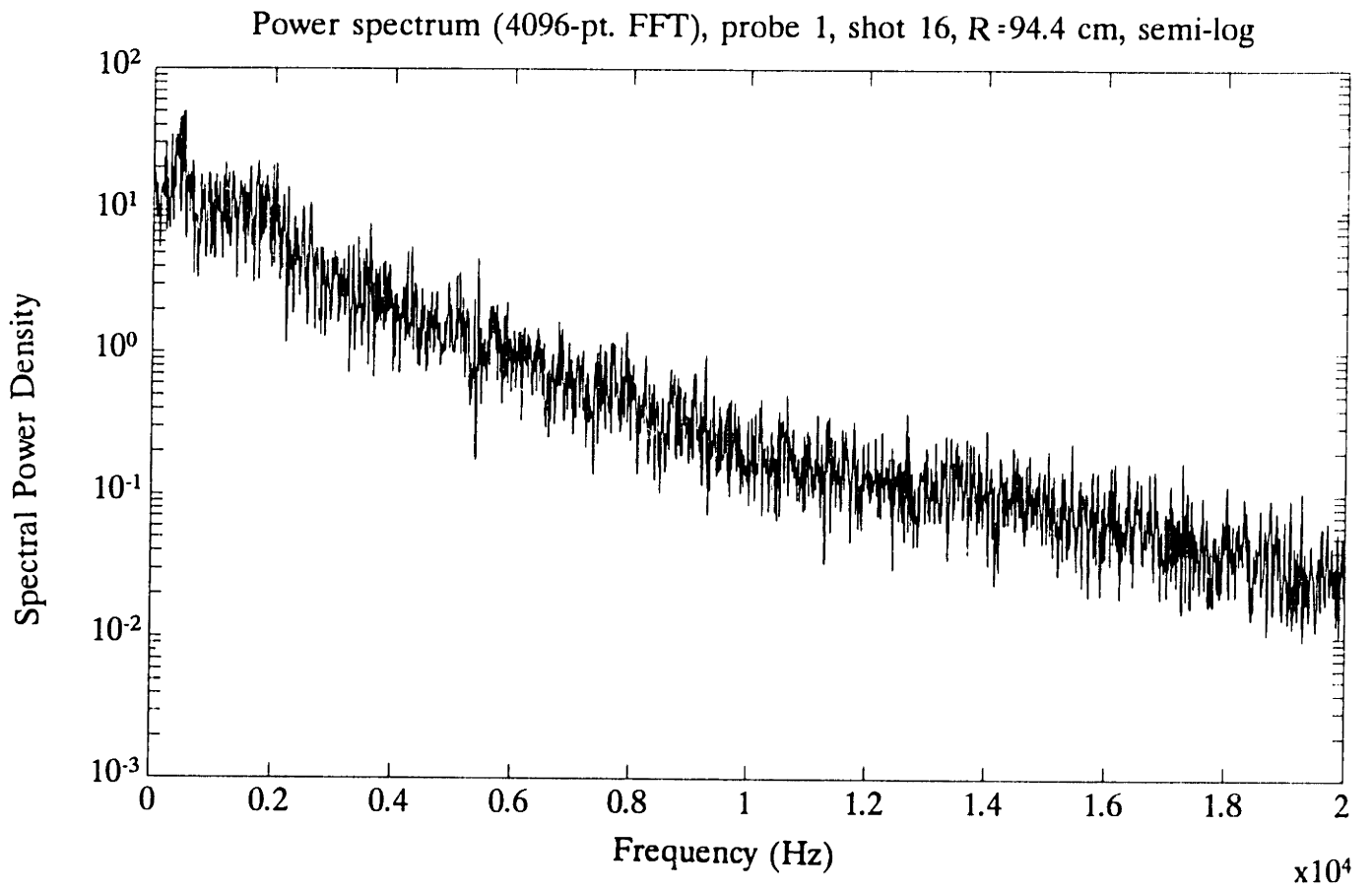
Figure A-3: Semi-logarithmic plot of fluctuation power spectrum. Major radius 94.4 cm.
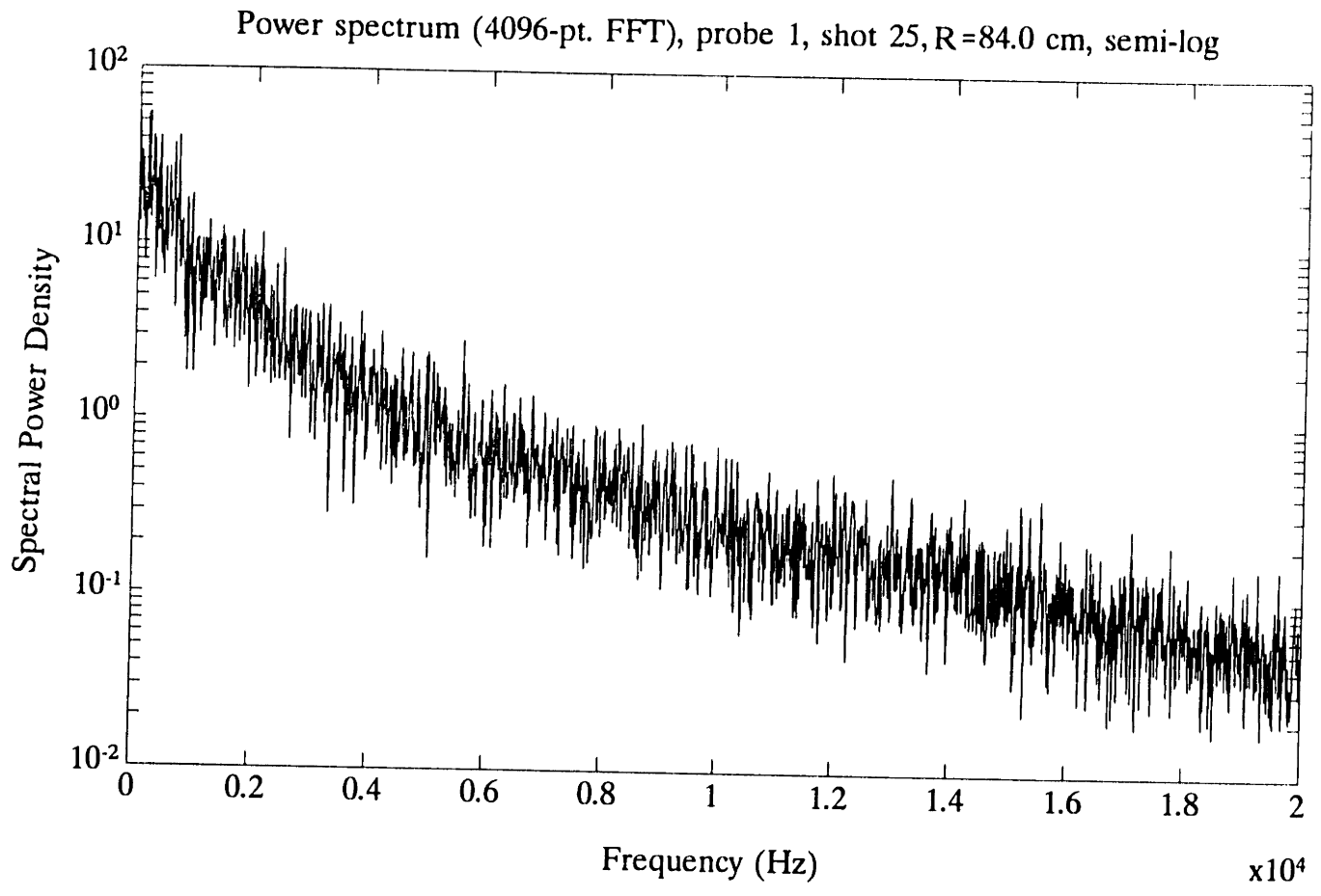
Figure A-4: semi-logarithmic plot of fluctuation power spectrum. Major radius 84.0 cm.

Appendix B

Coherence Functions of Selected Data Sets

This section contains plots of coherence function versus frequency for selected seta of data. Unlike the arrays used to generate the contour plots in Chapter 5, the coherence plots presented here were produced from 512-point FFTs.

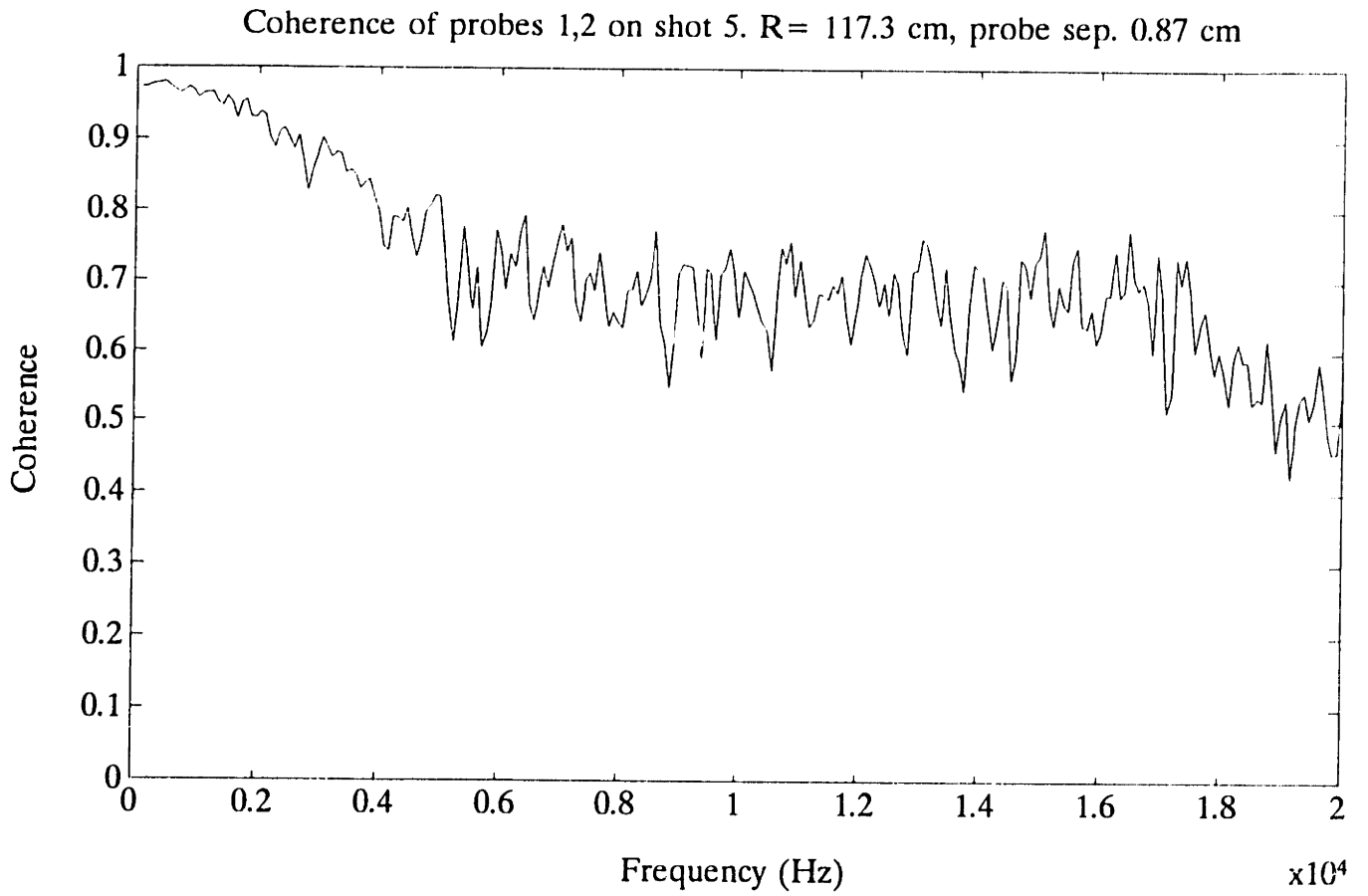Coherence of probes 1,2 on shot 5. R= 117.3 cm, probe sep. 0.87 cm

Figure B-1: Coherence between signals from probes 1 and 2 at major radius R= 117.3 cm. Probe separation 0.87 cm. Coherence is high at all frequencies.

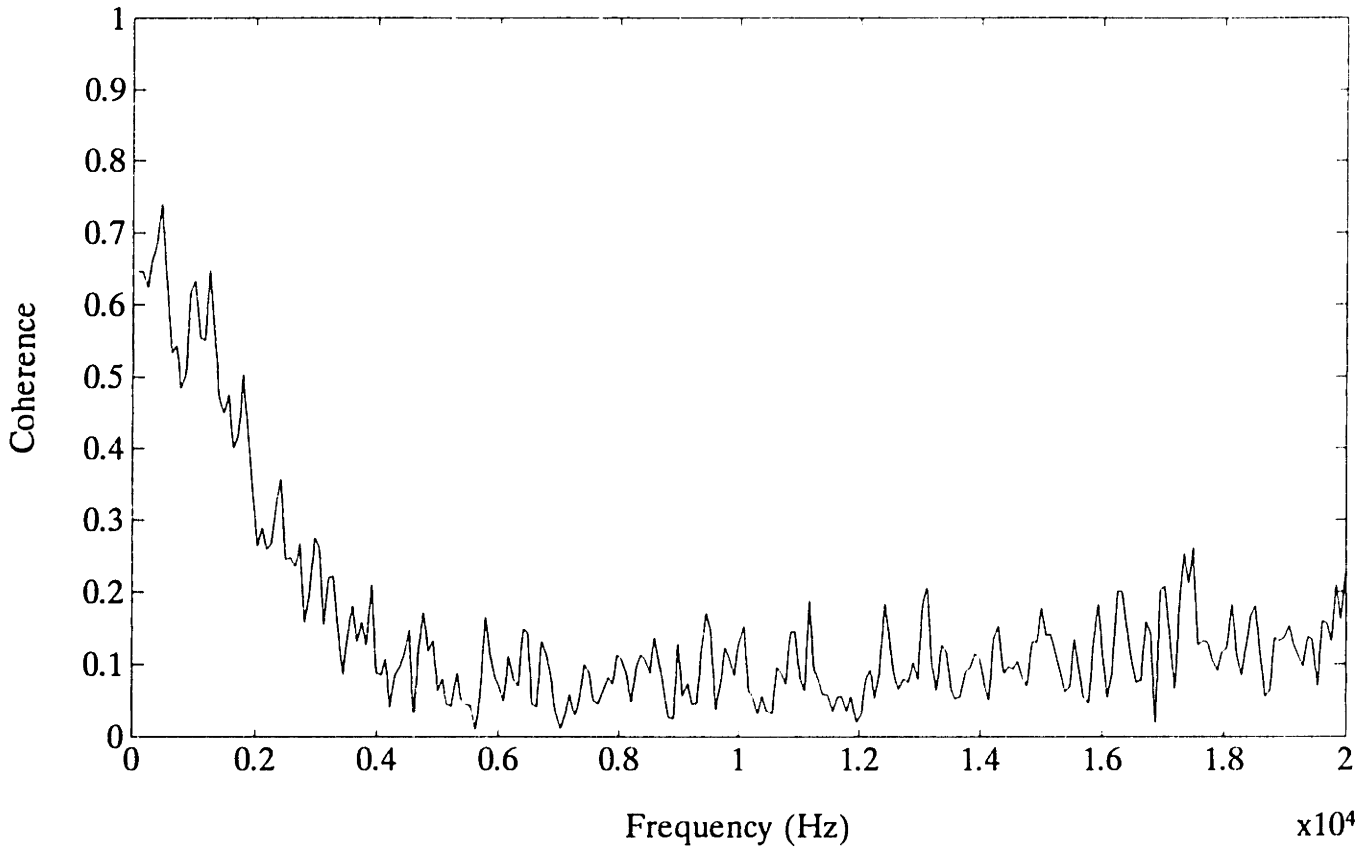Coherence of probes 1,10on shot 5. R = 117.3 cm, probe sep. 8.54 cm

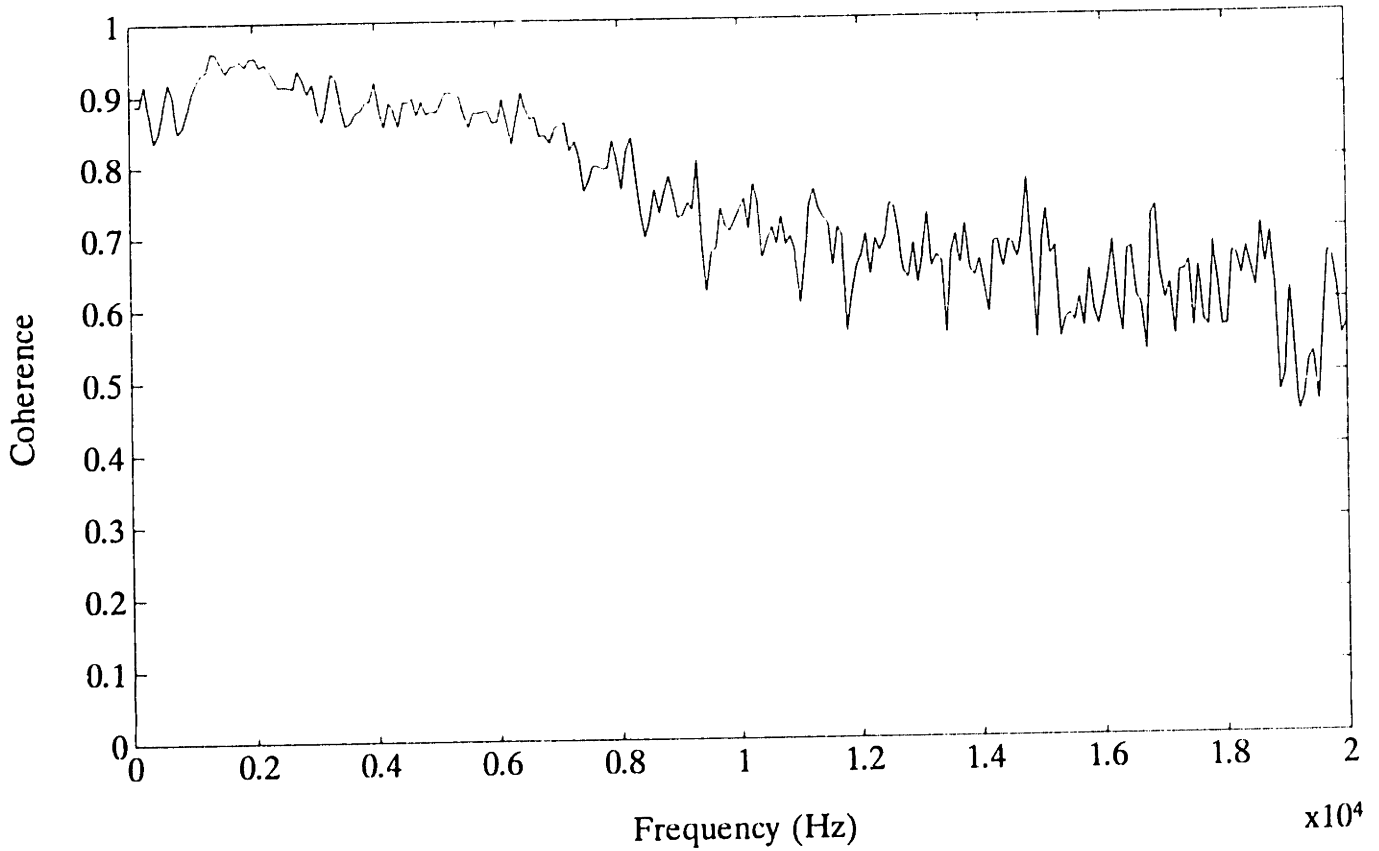Figure B-2: Coherence between signals from probes 1 and 10. R = 117.3 cm. Probe separation 8.54 cm. Coherence is low due to probe separation.

Figure B-3: Coherence between signals from probes 1 and 2. R = 94.4 cm. Probe separation 0.87 cm. High coherence.

Coherence of probes 1,10 on shot 17. R= 94.4 cm, probe sep. 8.54 cm
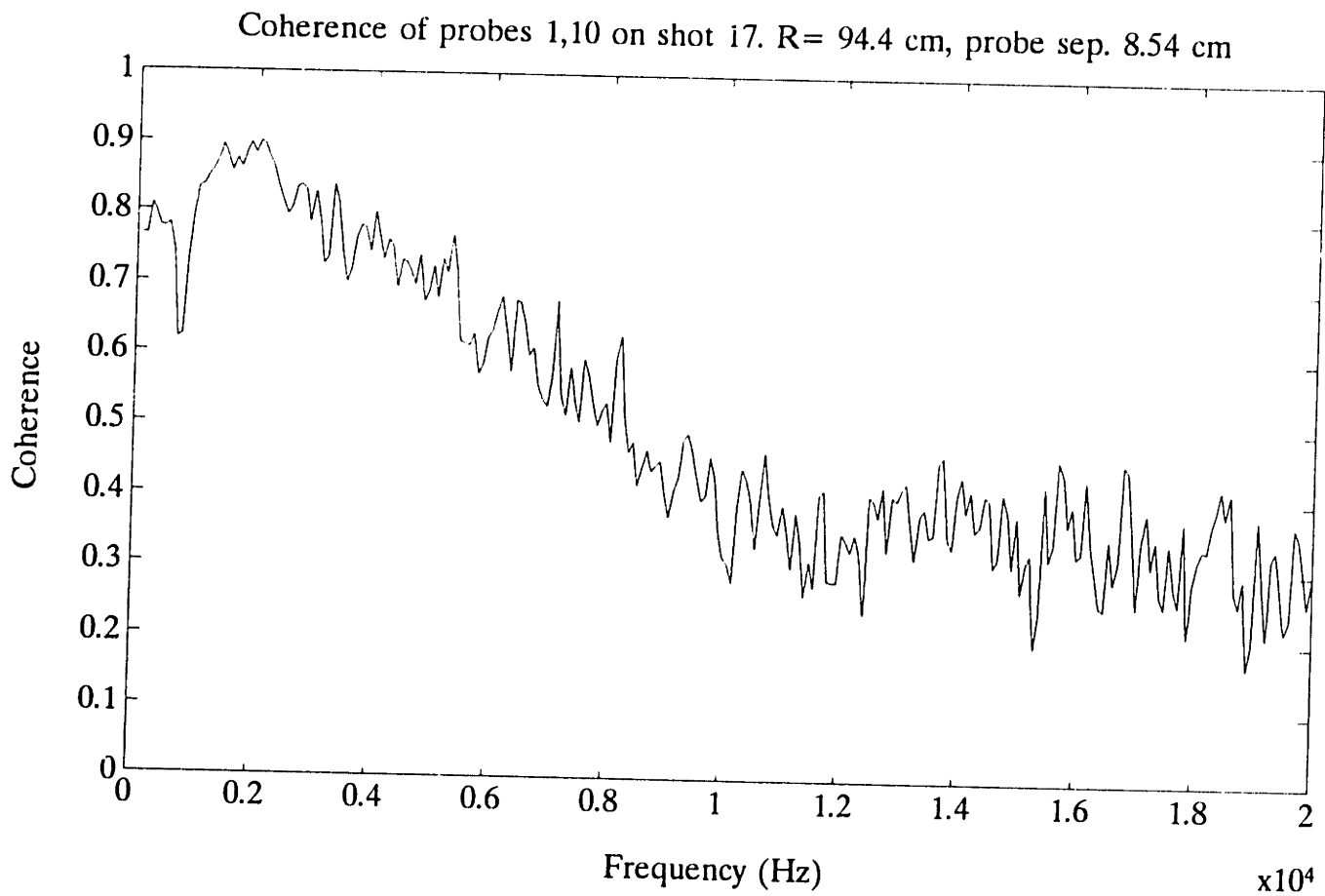
Figure B-4: Coherence between signals from probes 1 and 6. R = 94.4 cm. Probe separation 4.68 cm. Coherence is high due to apparent non-linearity of plasma.
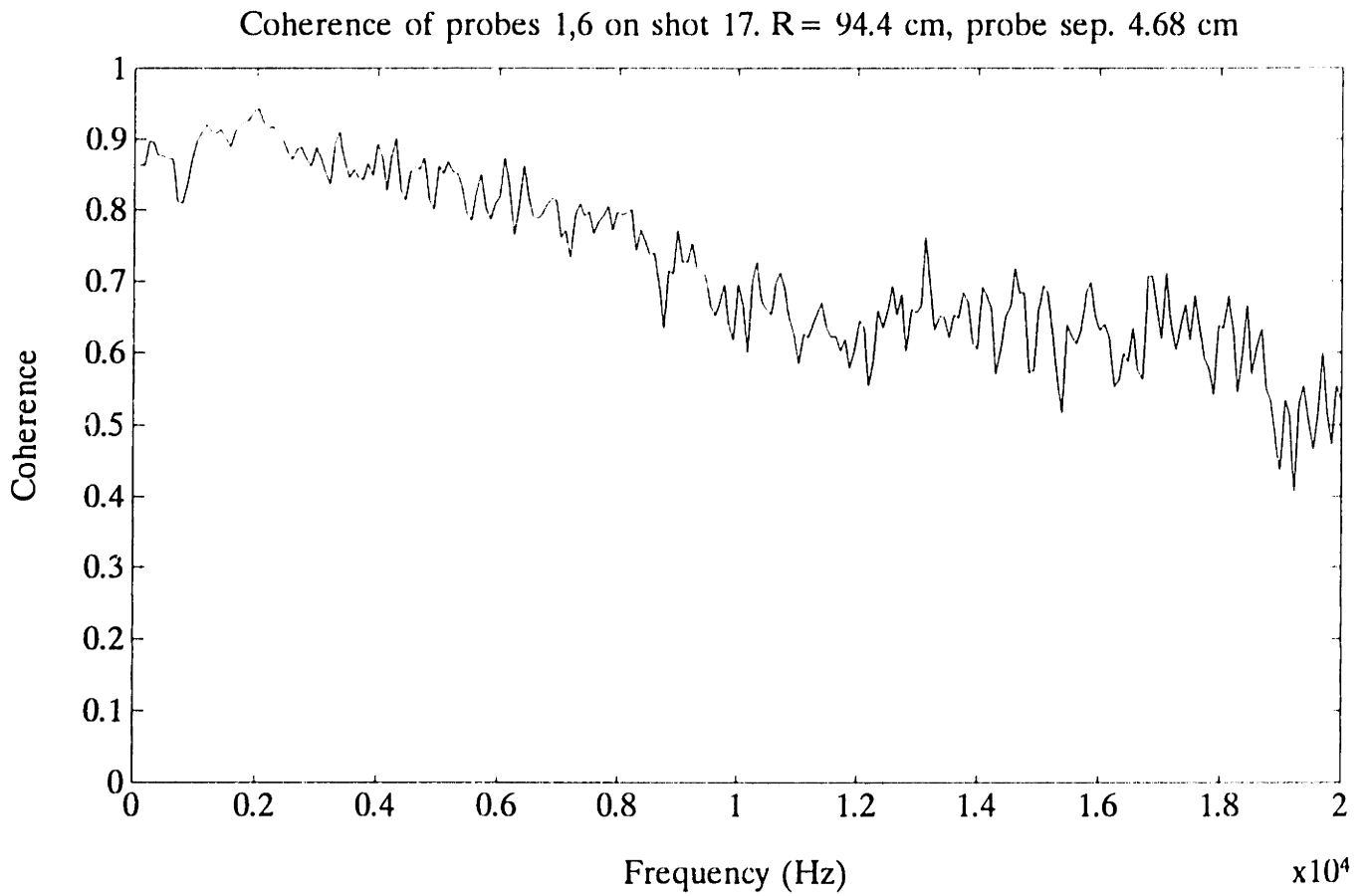
Coherence of probes 1,6 on shot 17. R = 94.4 cm, probe sep. 4.68 cm

Figure B-5: Coherence between signals from probes 1 and 10. R = 94.4 cm. Probe separation 8.54 cm. Coherence is lower.

91

Appendix C

MATLAB Code Written for Data Analysis

This appendix contains code which was written to be used with MATLAB numerical computation software. The FLUCSTAT program runs as a self-contained program which calls functions AVERUNV and VSCALE. Its purpose was to calculate the mean values of sets of data and to present both the average value and standard deviation. It calls VSCALE to scale the CAMAC's integer output to a voltage scale, and calls AVERUNV to print a graph on the screen showing the running average of the data array.

```
% Program FLUCSTAT.

% calculates the mean and estimated error of the floating potential

% (volts) based on the scaling in the function vscale.m


'Input array to be analyzed'

'c = data'

keyboard


vf = mean(vscale(c))


'vf is average potential in volts'


d = averunv(vscale(c),30);

err = std(d)/sqrt(30)


'err is estimated statistical error in vf'


pause


plot(d,'o')

title('Running average of data (volts)')
```

```
function y=vscale(c)


% Converts data taken from CAMAC to a voltage scale by assuming

% that channel # 2048 corresponds to zero, and that the full

% scale of 0-4096 corresponds to -5V to +5V.


y = c-(2048*ones(c));

y = y/409.6;
```

```
function y=averun(v,NB)



%

% This M-file computes the running average of a vector v.

%

% Number of data blocks in running average

% NB



y=0.0*[1:NB];

ND=length(v);



NI=floor(ND/NB);    %floor truncates data range if ND is not a multiple of NB.



'working ...'



   for kk=0:NB-1    % block index

    g = v((kk*NI)+1:((kk+1)*NI-1));



    y(kk+1)=mean(g);
```

```
    end

plot(y,'o')
```

Bibliography

Beals, D. F.: *Vacuum System Construction and Analysis for a TOKAMAK Plasma Device*, S. B. Thesis, Dept. of Mechanical Engineering, MIT, Cambridge, Mass., 1991.

Bendet, J., Piersol, A, *Random Data: Analysis and Measurement Procedures*, John Wiley and Sons, New York, 1986.

Chen, F. F.: *Introduction to Plasma Physics and Controlled Fusion*, 2d. ed., Plenum Press, New York, 1984.

Rost, J. C. *et al*, *Density and Potential Fluctuation Measurements in a Toroidal ECRH Sustained Plasma*, Poster, APS Plasma Physics Meeting, Seattle, November 1992.